MedVision: Benchmarking Quantitative Medical Image Analysis

Yongcheng Yao[1], Yongshuo Zong[1], Raman Dutt[1],
Yongxin Yang[2], Sotirios A Tsaftaris[1], Timothy Hospedales[1],

[1]University of Edinburgh, [2]Queen Mary University of London,
{yc.yao, yongshuo.zong, raman.dutt, s.tsaftaris, t.hospedales}@ed.ac.uk, yongxin.yang@qmul.ac.uk

Project: https://medvision-vlm.github.io

arXiv:2511.18676v2 [cs.CV] 6 Jun 2026

Abstract

Current vision-language models (VLMs) in medicine are primarily designed for categorical question answering (e.g., "Is this normal or abnormal?") or qualitative descriptive tasks. However, clinical decision-making often relies on quantitative assessments, such as measuring the size of a tumor or the angle of a joint, from which physicians draw their own diagnostic conclusions. This quantitative reasoning capability remains underexplored and poorly supported in existing VLMs. In this work, we introduce **MedVision**, a large-scale dataset and benchmark specifically designed to evaluate and improve VLMs on quantitative medical image analysis. MedVision spans 22 public datasets covering diverse anatomies and modalities, with **30.8 million** image-annotation pairs. We focus on three representative quantitative tasks: (1) detection of anatomical structures and abnormalities, (2) tumor/lesion (T/L) size estimation, and (3) angle/distance (A/D) measurement. We show that current off-the-shelf VLMs perform poorly on these tasks. However, supervised and reinforcement fine-tuning on MedVision significantly enhances performance across detection, T/L estimation, and A/D measurement. MedVision provides a foundation for developing VLMs with robust quantitative reasoning capabilities in medical imaging.

1 Introduction

Recent advances in vision-language models (VLMs) (Li et al., 2024a; Liu et al., 2023; Bai et al., 2023; Zong et al., 2024) have made it possible to pair powerful visual encoders with flexible natural language reasoning, enabling a range of clinical applications such as image-level classification and interactive question answering. In practice, however, most medical VLM usage and evaluation has concentrated on categorical (Lau et al., 2018; Liu et al., 2021; Ben Abacha et al., 2019) or qualitative outputs (Subramanian et al., 2020): distinguishing "normal vs abnormal" images, labeling a finding, or producing free-text descriptions of image content. These tasks are important, but they do not capture a critical part of routine clinical reasoning: the extraction of precise, *quantitative* measurements from images that clinicians use to stage disease, plan interventions, and monitor therapy.

Quantitative assessment is central to many medical decisions. Examples include detecting metastases and estimating tumor/lesion size for cancer staging (Eisenhauer et al., 2009; Detterbeck et al., 2024), and measuring cobb angle for scoliosis diagnosis (Cheng et al., 2015). Clinicians seldom make a diagnosis based solely on a binary label or qualitative description (e.g., "small tumor", "increased lesion size"); instead they combine measured quantities with clinical context to reach a conclusion. Despite this, the ability of modern VLMs to produce reliable, reproducible quantitative measurements (e.g., lengths, areas, volumes, angles) has received little systematic attention. Existing datasets (Lau et al., 2018; Ben Abacha et al., 2019, 2021; Liu et al., 2021; He et al., 2020a; Irvin et al., 2019; Chambon et al., 2024; Johnson et al., 2019; Kayser et al., 2022; Boecking et al., 2022; Lin et al., 2023) emphasize classification accuracy or natural language quality rather than measurement precision. Recently, RadGPT (Bassi et al., 2025) presents a dataset of radiology reports with tumor location and size information, but it is limited to abdomen CT scans. Related benchmarks (Ye et al., 2024; Hu et al., 2024; Wu et al., 2025; Zhou et al., 2025) similarly focus on qualitative tasks, such as image modality recognition, disease classification, visual question answering, and report generation. Off-the-shelf VLMs are rarely evaluated on tasks that require exact spatial localization and numerical outputs. A recent work on reinforcement fine-tuning, MedVLM-R1 (Pan et al., 2025), improves medical VLM accuracy on classification tasks, but leaves quantitative measurement largely unaddressed. A

detailed comparison of existing datasets and benchmarks is provided in Appendix A.

There are several reasons why quantitative vision–language capability is both challenging and underexplored. First, measurement tasks demand precise localization (often at sub-pixel or small-structure scales) and robust handling of modality-specific image characteristics (CT, MRI, X-ray, ultrasound). Second, producing correct measurements requires the model to understand geometric relationships and physical units, not just semantic categories. Third, public datasets with standardized, high-quality measurement annotations are sparse or fragmented across modalities and anatomies, making large-scale evaluation and model training difficult. Finally, many VLM architectures and training objectives are not designed to produce calibrated numeric outputs or to combine localized visual evidence with explicit numeric reasoning.

To address these gaps, we introduce **MedVision**, a large-scale dataset and benchmark specifically created to assess and improve VLM performance on quantitative medical-image tasks. MedVision aggregates *22* public datasets spanning multiple anatomies and imaging modalities, comprising **30.8 million** images with rich, structured annotations suitable for measurement tasks. We organize the benchmark around three representative, clinically relevant tasks: (1) detection of anatomical structures and abnormalities (localization and identification), (2) tumor/lesion (T/L) size estimation (bidirectional dimensions), and (3) angle/distance (A/D) measurement (e.g., joint angles, inter-structure distances). These tasks capture the range of quantitative demands found in routine radiology and specialty workflows.

Using MedVision, we perform a systematic evaluation of open-weight VLMs in two settings: off-the-shelf inference and fine-tuning on the MedVision training splits. Our benchmarks show that off-the-shelf VLMs, even those with strong qualitative language abilities, perform poorly on quantitative tasks, failing at precise localization and producing large numeric errors. We then demonstrate that targeted supervised and reinforcement fine-tuning (SFT+RFT) on MedVision materially improves model performance across detection metrics (recall, precision, F1, IoU) and measurement accuracy (reduced absolute and relative errors for size and angle/distance). Notably, MedVision-V0, our 7B fine-tuned model, significantly outperforms all evaluated off-the-shelf VLMs. Alongside quantitative results, we analyze common failure modes and identify persistent challenges that future research must address. To summarize, our main contributions are as follows:

(i) We highlight a clinically important but underappreciated gap: modern VLMs are not reliably able to produce precise quantitative measurements from medical images.

(ii) We introduce **MedVision**, a large-scale, multi-modality dataset for quantitative medical image analysis.

(iii) We provide the first comprehensive evaluation of contemporary VLMs on detection, tumor/lesion size estimation, and angle/distance measurement.

(iv) We train **MedVision-V0** on our dataset via supervised and reinforcement learning, which significantly outperforms all evaluated VLMs across all three quantitative tasks, establishing a strong open baseline for future research.

(v) We release the data, model checkpoints, and code (training and evaluation) to enable further research toward VLMs that support clinically useful quantitative reasoning.

2 MedVision: Dataset and Benchmark

An overview of our MedVision dataset and benchmark design is illustrated in Figure 1. We curated a large-scale multi-anatomy and multi-modality medical image dataset with quantitative annotations (Section 2.1). We designed a benchmark to evaluate VLMs' ability on three quantitative medical image analysis tasks (Section 2.2). The benchmark is conducted in the form of open-ended VQA. We convey physical spacing information (i.e., pixel size) in the text prompt to provide VLMs with the necessary context for quantitative analysis tasks.

2.1 Dataset

We constructed the MedVision dataset from public medical image data. Quantitative annotations are derived from the original labels. The dataset construction process is automated and reproducible, with a codebase that handles raw data downloading, image preprocessing, and annotation extraction.

Data Source & Preprocessing. Public medical imaging data with segmentation masks or landmark annotations were collected. We restricted the medical image modalities to those with physical spacing information in the image file header, which is essential for generating ground truth quantitative mea-

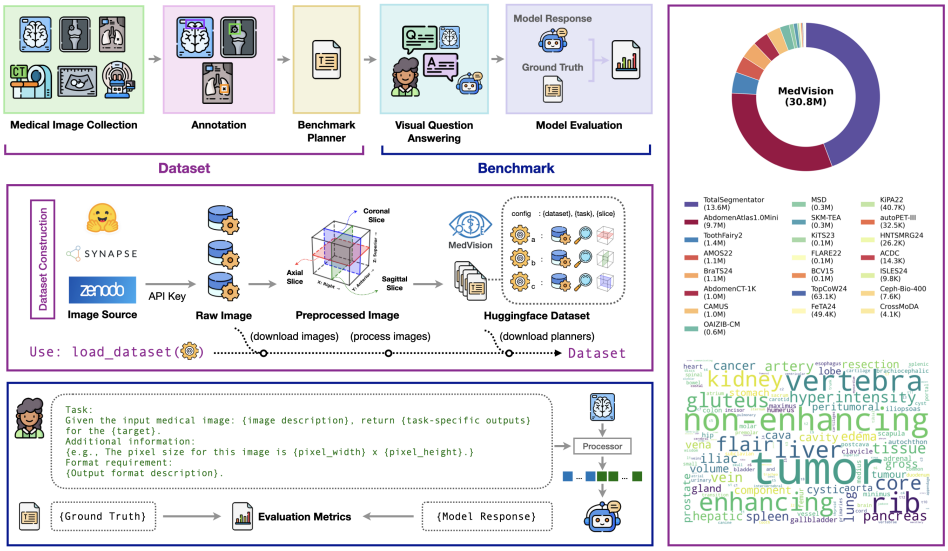


Figure 1: Overview of MedVision dataset construction and benchmark design (left), and dataset summary (right). The MedVision dataset was constructed for out-of-the-box use: `load_dataset` is all you need. Appendix B shows examples of imaging data and quantitative annotation.

surements. We collected 22 datasets, summarized in Table 1, covering a diverse range of anatomies and modalities: AbdomenAtlas (Li et al., 2024b), AbdomenCT-1K (Ma et al., 2022), ACDC (Bernard et al., 2018), AMOS22 (Ji et al., 2022), autoPET-III [1], BCV15 [2], BraTS24 (de Verdier et al., 2024; LaBella et al., 2025; Kazerooni et al., 2024), CAMUS (Leclerc et al., 2019), Ceph-Bio-400 (Lindner et al., 2016), CrossModDA (Dorent et al., 2023), FeTA24 (Payette et al., 2023), FLARE22 (Ma et al., 2024), HNTSMRG24 [3], ISLES24 [4], KiPA22 (He et al., 2021, 2020b; Shao et al., 2011, 2012), KiTS23 (Heller et al., 2023), MSD (Antonelli et al., 2022), OAIZIB-CM (Ambellan et al., 2019; Yao et al., 2024; Yao and Chen, 2025), SKM-TEA (Desai et al., 2022), ToothFairy2 (Bolelli et al., 2025, 2024; Lumetti et al., 2024), TopCoW24 (Yang et al., 2025), and TotalSegmentator (Wasserthal et al., 2023). Images are preprocessed to ensure consistent orientation and standardized format. Images are stored as 3D volumes with orientation corrected to RAS+ convention, where the first, second, and third dimensions correspond to the left-to-Right, posterior-to-Anterior, and inferior-to-Superior directions, respectively. Our data loading codebase supports flexible image slicing along any of the three anatomical planes (sagittal, coronal, and axial).

Quantitative Annotations. We generated bounding box (b-box), bidirectional tumor/lesion (T/L) size, and angle/distance (A/D) annotations to support the three benchmark tasks. The new annotations and metadata of images are released as benchmark planner. ***(i) Bounding Box Annotation:*** For each segmentation label in a 2D slice, a bounding box is fitted to each cluster of the binary mask. Clusters with fewer than 10 pixels in any dimension are excluded. ***(ii) Tumor/Lesion Size Annotation:*** Bidirectional measurements of tumors/lesions from medical images are useful metrics and can provide quantitative information for disease assessment and monitoring. We generated T/L size annotations by calculating the lengths of the major and minor axes of the fitted ellipse to each T/L label in 2D slices (Figure 2). Ellipse fitting is conducted in the real-world coordinate system by multiplying the image array indices with pixel sizes, so that the fitting process takes into account the physical spacing and results in accurate measuring directions (i.e., major and minor axes). Fitted ellipses whose endpoints are outside the buffer zone between the 10% shrunk and enlarged bounding boxes of the target region are excluded to avoid unreliable annotations. The physical lengths and endpoint coordinates of the major and minor axes are recorded in the T/L task planner. ***(iii) Angle/Distance Annotation:*** Angle and distance measurements are calculated from human-annotated landmarks. We

[1] https://autopet-iii.grand-challenge.org
[2] https://doi.org/10.7303/syn3193805
[3] https://hntsmrg24.grand-challenge.org
[4] https://isles-24.grand-challenge.org

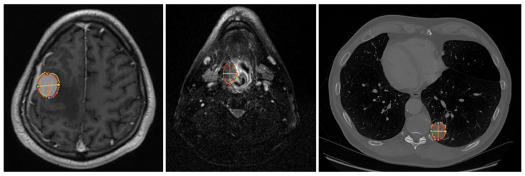


Figure 2: Tumor/lesion size annotation. An ellipse is fitted to the tumor/lesion mask. The physical lengths of the major and minor axes are recorded as T/L size annotation.

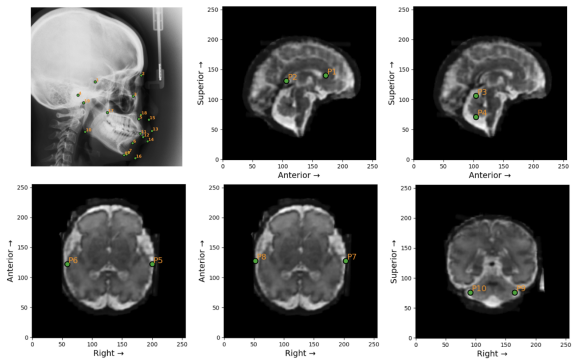


Figure 3: Landmarks in the Ceph-Bio-400 (top-left) and FeTA24 datasets. Ground truth angle and distance measurements are calculated from these landmarks.

generated standardized annotations in the format of landmark coordinates and landmark/angle/distance maps, where each measurement is well-defined and can be calculated from landmark coordinates. Figure 3 shows examples of landmarks in the two datasets.

Real-World Units. Importantly, MedVision annotations are in clinically-relevant real-world units such as `mm` rather than simplistic `pixels`. This is important for producing a clinically relevant generalist model, and for a self-consistent multi-dataset benchmark suite, because different individual datasets/images have different real-world pixel sizes. MedVision benchmark competitors must perform arithmetic to translate image-wise pixel size to real-world units.

Dataset Release. MedVision dataset (v1.0.0) contains 30.8 million image-annotation pairs across 22 data sources and 3 tasks. For each task, we randomly split the data into training (70%) and test sets (30%) at the subject level. In this study, we use the training set for model fine-tuning and test set for evaluation. It supports reproducible dataset construction and automated loading. Users can get started with a single `load_dataset()` call with a specified data configuration (dataset + task + plane).

Table 1: Details of the MedVision dataset. MRI: Magnetic Resonance Imaging; CT: Computed Tomography; PET: positron emission tomography; US: Ultrasound; b-box: bounding box; T/L: tumor/lesion size; A/D: angle/distance. Full statistics in Table 10 (Appendix C).

Dataset	Anatomy	Modality	Annotation
AbdomenAtlas	abdomen	CT	b-box
AbdomenCT-1K	abdomen	CT	b-box
ACDC	heart	MRI	b-box
AMOS22	abdomen	CT, MRI	b-box
autoPET-III	whole body	CT, PET	b-box, T/L
BCV15	abdomen	CT	b-box
BraTS24	brain	MRI	b-box, T/L
CAMUS	heart	US	b-box
Ceph-Bio-400	head and neck	X-ray	b-box, A/D
CrossModDA	brain	MRI	b-box
FeTA24	fetal brain	MRI	b-box, A/D
FLARE22	abdomen	CT	b-box
HNTSMRG24	head and neck	MRI	b-box, T/L
ISLES24	brain	MRI	b-box
KiPA22	kidney	CT	b-box, T/L
KiTS23	kidney	CT	b-box, T/L
MSD	multiple	CT, MRI	b-box, T/L
OAIZIB-CM	knee	MRI	b-box
SKM-TEA	knee	MRI	b-box
ToothFairy2	tooth	CT	b-box
TopCoW24	brain	CT, MRI	b-box
TotalSegmentator	multiple	CT, MRI	b-box

2.2 Benchmark

Model. We evaluated a range of general and medical open-weight VLMs. General VLMs include Qwen2.5-VL (Bai et al., 2025), InternVL3 (Zhu et al., 2025), Gemma3 (Team et al., 2025a), Llama3.2-Vision and LLaVA-OneVision (Li et al., 2024a). Medical VLMs include Lingshu (Team et al., 2025b), MedGemma (Sellergren et al., 2025), MedDr (He et al., 2026), HuatuoGPT-Vision (Chen et al., 2024), and HealthGPT-L14 (14B) (Lin et al., 2025). Details of these models are provided in Appendix D.

Prompt. We focus on clinically related open-ended VQA tasks for our benchmark: (1) healthy anatomical structures and abnormalities detection, (2) tumor/lesion size estimation, and (3) angle/distance measurement. Models are instructed to output the required estimates in a structured format. Generally, for all tasks, the input prompt includes task description and format requirement. Specifically, for T/L and A/D tasks, physical spacing information and chain-of-thought (CoT) instructions are added to provide necessary context and guide the model's reasoning process. ***(i) Physical Spacing Information:*** A key feature of the benchmark is the careful handling of physical spacing information in the text prompt. Since each VLM adapts different image processing strategies (see Appendix E), we design a dedicated prompt-building pipeline to ensure the physical spacing values provided in the prompt match the actual image input. Specifically, in every image resizing step, we update the pixel

size accordingly, so that the image size and pixel size together always reflect the physical dimensions of the target region. ***(ii) CoT Instruction:*** The CoT instruction for T/L and A/D tasks provides step-by-step guidance for specific measurement tasks. In general, it instructs the model to first estimate landmark coordinates, then calculate the target distance or angle based on the predicted coordinates and the provided physical spacing information.

Metric. Model responses are parsed to extract the required numerical values. Parsing success is determined by whether the model output the required number of numerical values within the `<answer></answer>` tags. Success rate (SR) is calculated as the proportion of successfully parsed outputs among all samples. Only successfully parsed outputs are included in the calculation of other metrics. Notably, for the `<metric>`$_{<k}$ or `<metric>`$_{>k}$ metrics, the denominator is the total number of samples, so that it reflects both instruction following and measurement accuracy. For detection tasks, we report the region-based recall, precision, F1 score, and intersection over union (IoU), and IoU$_{>0.5}$. For T/L size and A/D measurement tasks, we report the mean absolute error (MAE), mean relative error (MRE), and MRE$_{<0.1}$. Metric definitions are provided in Appendix F.

Experimental Setting. Details on computational resources, software environment, and code release are provided in Appendix G.

3 MedVision-V0 Training

We established the MedVision benchmark to evaluate VLMs' capabilities on quantitative medical image analysis tasks. Our results reveal that pre-trained models struggle with medical image quantification. This performance gap motivates the need for post-training on our dataset. We aim to train a model capable of anatomical structure recognition, precise localization, tumor/lesion size estimation, and measurement via internal perception and reasoning – an end-to-end VLM that does not rely on external tools or specialist models. To achieve this, we adopted a two-stage fine-tuning strategy, which includes supervised fine-tuning (SFT) and reinforcement learning fine-tuning (RFT). The SFT stage focuses on teaching the model to learn the answer formats and reasoning patterns, while the RFT stage further refines the model's outputs based on task-specific reward functions that encourage accurate intermediate estimates (e.g., landmark coordinates) and final measurements. We denote our model **MedVision-V0**.

SFT with CoT. At this stage, we curated a multi-task CoT dataset with 121K samples from the MedVision training set. We randomly select 110K detection, 5.5K T/L size estimation, and 5.5K A/D measurement cases from a subset of axial slices. We deliberately leave out coronal and sagittal slices to evaluate the model's generalization ability to out-of-distribution (OOD) data. A weighted random sampler is used during training to allow oversampling of minority-task cases to mitigate the data imbalance issue. Each sample includes an image reshaped to 512x512 and a prompt-answer pair. The prompt follows the same format as the one used in the benchmark. The answer is structured into an internal reasoning part wrapped in `<think></think>` tags and a final answer in `<answer></answer>` tags. The reasoning text is generated by filling in intermediate ground truth values (e.g., landmark coordinates) into the task-specific CoT instruction template.

RFT via GRPO. For RFT, we used the GRPO algorithm (Shao et al., 2024) implemented in verl (Sheng et al., 2025). We constructed RFT dataset for each of the three tasks and used them sequentially (A/D $\rightarrow$ T/L $\rightarrow$ detection) for multi-step fine-tuning. The same 121K training samples from the SFT stage are used; the image size and prompt remain the same, while the CoT answer is removed in RFT data as models learn from reward signal. In addition to the standard format and answer rewards in GRPO, we designed process rewards for T/L and A/D tasks to encourage accurate intermediate estimates. Both the process and answer rewards are calculated from $\exp(-x)$ where x is the error of model prediction. The final reward is calculated as follows: $r = r_{\text{format}} + r_{\text{process}} * r_{\text{answer}}$.

4 Results & Analysis

We first provide an overview of our fine-tuned model, MedVision-V0, and then quantitatively compare the performance of all evaluated models on the three benchmark task families.

4.1 MedVision-V0 Overview

Qualitative Overview. Figure 4 shows an example of brain tumor size estimation by MedVision-V0. The model is able to correctly identify the tumor region and produce reasonable estimates. The model's internal reasoning process, as reflected in

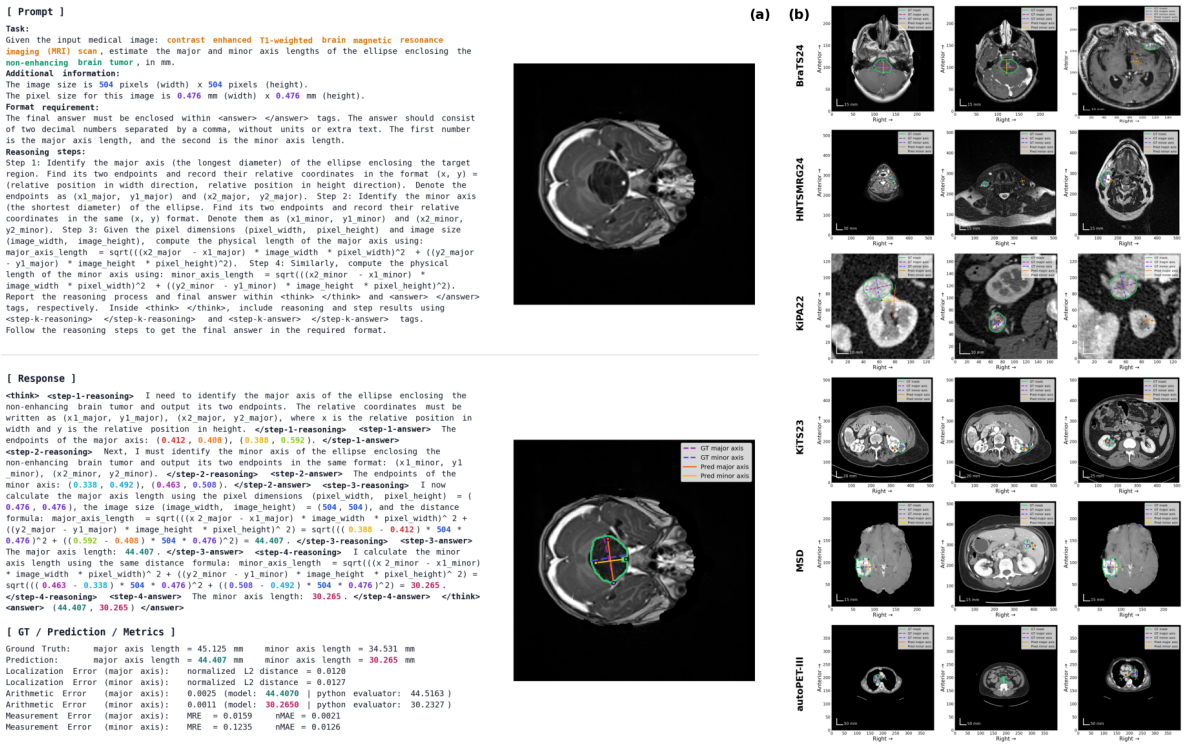


Figure 4: Example query and responses from MedVision-V0 on T/L size estimation task. (a) Prompt, input image, response, and error analysis of an example of brain tumor size estimation. (b) Random samples of model responses.

the <think></think> tags, shows that it first estimates the *relative coordinates* of endpoints, then calculates the lengths based on these coordinates and the provided pixel size and image size. More examples of model responses in detection and A/D tasks are provided in Appendix H.

Error Analysis. To understand the challenge posed by MedVision, we analyse the end-to-end measurement error against the error of sub-tasks along the reasoning path: i) landmark localization, and ii) arithmetic mapping landmark locations to final answers. We quantify the ***localization error*** by the normalized L2 distance, $\|(x_1 - x_2, y_1 - y_2)\|_2/\sqrt{2} \in [0, 1]$, where $(x_1, y_1), (x_2, y_2)$ are relative coordinates. The model learns to use the standard formula to calculate a distance or angle. To analyze the ***arithmetic error***, we calculate the MRE between the model's prediction and the output of a Python execution of the same formula. The arithmetic error reflects the model's ability to perform the calculation, independent of the localization error. The final ***measurement error*** is a coupling of the localization and arithmetic errors. Table 2 shows that the localization of tumor/lesion landmarks is more challenging than that of anatomical landmarks in angle/distance tasks, since the former involves irregular and variable structures. However, the arithmetic error is higher in A/D tasks, due to the more complex calculation of angles than distances.

Table 2: MedVision-V0 error analysis on A/D and T/L tasks. normL2: normalized L2 distance; MRE: mean relative error; reported in %.

Task	Localization (normL2)	Arithmetic (MRE)	Measurement (MRE)
A/D	1.6	12.8	27.6
Ceph-Distance	1.4	1.4	5.4
Ceph-Angle	1.6	25.9	52.1
FeTA-Distance	3.1	2.1	15.8
T/L	6.0	3.4	26.0

Performance. Summary metrics for all evaluated models on all tasks are given in Section 4.2. Here we provide a more detailed breakdown of MedVision-V0's performance on the detection (Table 3) and T/L tasks (Table 4). The model performs better on anatomical structure than tumor/lesion detection. The relative error of lesion size estimation ranges from 13% to 33%. Label-level detection performance and the effect of target size on detection, are provided in Appendix I, where it shows that small targets and tumor/lesion detection are more challenging.

Table 3: Detection performance of MedVision-V0, with the original labels categorized into 26 groups. Metrics are reported in %. R: recall; P: precision; F1: F1 score; IoU: intersection over union; SR: success rate.

Label	R ↑	P ↑	F1 ↑	IoU ↑	SR ↑	$IoU_{>0.5}$ ↑
Anatomy (18 regions, 13.4K samples)						
Knee Bone @ MR	96.3	97.2	96.7	94.3	100	99.2
Spleen @ CT	96.1	93.3	94.3	90.4	100	98.0
Liver @ CT	93.3	91.7	91.9	88.0	100	94.9
Kidney @ CT	92.2	92.3	91.8	87.4	100	95.8
Artery @ CT	91.8	90.3	90.8	85.3	100	97.3
Stomach @ CT	87.5	91.4	88.5	82.3	100	93.0
Heart @ US	83.5	88.9	85.0	76.1	100	91.6
Vein @ CT	75.3	75.4	73.3	65.6	100	76.2
Pancreas @ CT	74.0	79.3	73.2	62.6	100	74.5
Brain @ MR	72.6	74.0	70.2	61.0	100	67.2
Heart @ MR	78.7	68.1	70.2	60.7	100	67.5
Gallbladder @ CT	72.8	71.7	69.5	60.4	100	68.9
Prostate @ MR	84.4	59.1	66.3	55.2	100	62.7
Esophagus @ CT	58.1	58.1	56.9	45.1	100	44.1
Knee Soft Tissue @ MR	59.0	58.8	54.8	44.2	100	47.9
Artery @ MR	63.9	51.7	54.8	44.9	100	51.5
Intestine @ CT	57.5	60.3	52.9	39.8	100	33.3
Adrenal Gland @ CT	31.5	33.2	29.8	20.2	100	10.2
Tumor/Lesion (8 regions, 8.5K samples)						
Kidney Tumor/Lesion @ CT	51.2	64.4	53.4	43.9	100	47.7
Liver Tumor/Lesion @ CT	53.3	58.0	50.9	41.6	100	46.2
Brain Tumor/Lesion @ MR	55.4	51.3	48.6	39.5	100	42.0
Colon Tumor/Lesion @ CT	41.3	44.3	40.2	33.5	100	35.7
Head-Neck Tumor/Lesion @ MR	57.6	38.7	40.1	33.0	100	34.4
Pancreas Tumor/Lesion @ CT	51.0	35.4	38.8	27.9	100	18.8
Lung Tumor/Lesion @ CT	37.8	42.0	37.5	30.6	100	33.4
Metastatic Lymph Node @ MR	41.4	37.0	36.7	30.4	100	33.5

Table 4: T/L size estimation performance of MedVision-V0.

Label	MAE ↓	MRE ↓	SR ↑	$MRE_{<0.1}$ ↑
enhancing brain tumor @ MR	5.2	13.1	100.0	53.6
non-enhancing brain tumor @ MR	6.0	19.6	100.0	38.4
brain resection cavity @ MR	7.8	20.5	100.0	32.5
brain tumor @ MR	6.2	22.3	100.0	38.4
kidney tumor @ CT	12.5	27.5	100.0	18.4
metastatic lymph node @ MR	6.2	28.3	100.0	17.5
liver tumor @ CT	16.4	33.1	100.0	19.5

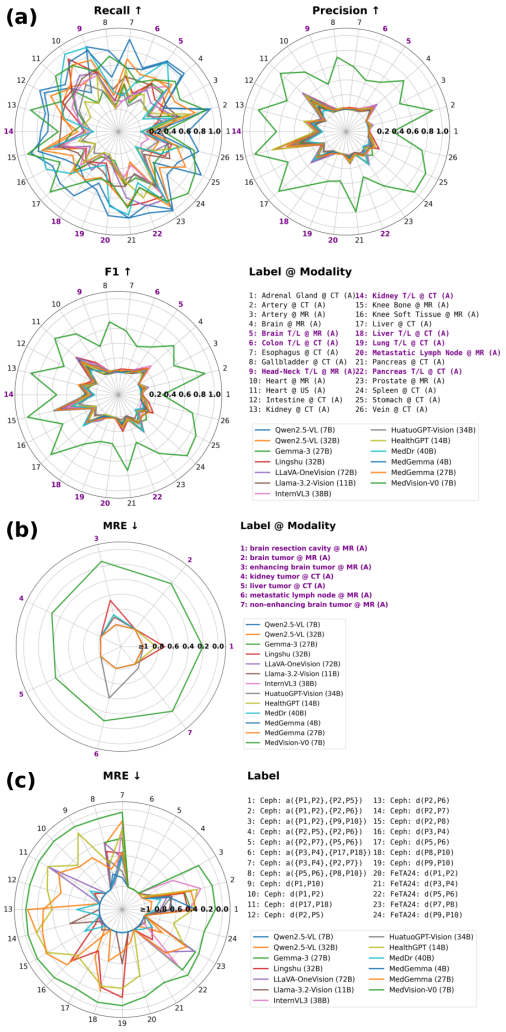


Figure 5: Performance of evaluated models on the three benchmark tasks.

4.2 Comparative Benchmarking Results

We compare MedVision-V0 with 12 other VLMs on the three task families. The results are visualized in Figure 5 and detailed in Tables 5, 6, and 7. MedVision-V0 shows superior performance across these tasks, demonstrating the effectiveness of our SFT-RFT training strategy. Among the off-the-shelf models, medical VLMs show better zero-shot performance than general-purpose VLMs, likely due to their exposure to medical data. However, the second-best models (e.g., Lingshu and HealthGPT-L14) fail in lesion size estimation and angle measurement tasks (with MRE $> 100\%$). This reveals the limitation of both cutting-edge, general-purpose VLMs and specialised medical VLMs for quantitative medical image analysis, highlighting the value of our benchmark/dataset and the need for further research in this area.

4.3 Effectiveness of SFT-RFT Training

We study the impact of our training pipeline by comparing our base model with SFT and SFT-RFT post-training on MedVision.

In-distribution. SFT dramatically improves detection precision, T/L size estimation, and A/D measurement accuracy over the base model; the additional RFT step yields further consistent gains across all tasks (Table 13 in Appendix H).

Out-of-distribution Generalization. Both SFT and SFT-RFT models generalize to unseen imaging planes (plane-OOD) and unseen anatomical targets (target-OOD), with MedVision-V0 consistently outperforming the SFT-only model across detection and T/L size estimation (Table 14 in Appendix H).

Table 5: Model performance on detection tasks. Labels are categorized into anatomy and tumor/lesion groups. Metrics are reported in %.

Model	R ↑	P ↑	F1 ↑	IoU ↑	SR ↑	$IoU_{>0.5}$ ↑
Anatomy (18 regions, 13.4K samples)						
MedVision-V0 (7B)	81.3	80.4	79.1	72.0	100	80.1
Lingshu (32B)	37.4	20.2	20.2	13.7	100	6.7
MedGemma (27B)	56.4	15.5	18.8	12.7	97.1	6.6
MedGemma (4B)	68.6	14.6	18.5	12.4	98.2	6.4
Qwen2.5-VL (32B)	44.8	14.9	18.4	12.5	100	6.3
LLava-OneVision (72B)	34.9	19.0	18.1	11.8	100	2.4
InternVL3 (38B)	31.1	17.0	17.2	11.5	100	5.3
Qwen2.5-VL (7B)	69.6	12.2	16.7	11.3	99.3	5.6
Gemma3 (27B)	37.1	12.4	14.9	10.1	100	4.6
HealthGPT-L14 (14B)	27.3	19.4	14.9	9.5	92.0	1.7
MedDr (40B)	53.2	11.1	14.6	9.6	96.2	4.1
HuatuoGPT-Vision (34B)	21.2	14.1	12.3	8.0	80.0	2.2
Llama3.2-Vision (11B)	41.9	8.6	10.7	7.1	70.1	2.5
Tumor/Lesion (8 regions, 8.5K samples)						
MedVision-V0 (7B)	52.4	50.5	46.9	38.2	100	40.7
Lingshu (32B)	40.2	6.0	8.6	5.1	100	0.2
LLava-OneVision (72B)	34.1	6.3	8.4	5.0	100	0.4
InternVL3 (38B)	29.5	6.6	7.9	4.9	100	0.8
Qwen2.5-VL (32B)	38.5	5.7	7.7	4.7	100	0.6
MedGemma (27B)	52.7	4.5	7.4	4.2	94.4	0.1
MedGemma (4B)	77.6	4.4	7.4	4.2	99.1	0.0
HealthGPT-L14 (14B)	25.6	5.9	7.1	4.4	82.6	0.5
Qwen2.5-VL (7B)	77.4	3.8	6.5	3.6	99.6	0.0
MedDr (40B)	63.2	3.7	6.2	3.5	98.5	0.1
Gemma3 (27B)	34.3	4.3	6.1	3.6	100	0.3
HuatuoGPT-Vision (34B)	17.8	4.0	5.1	3.1	76.6	0.3
Llama3.2-Vision (11B)	43.4	2.3	3.8	2.1	68.6	0.0

Table 6: Model performance on tumor/lesion size estimation tasks. MRE, SR, and $MRE_{<0.1}$ are reported in %, while MAE is in millimeters.

Model	MAE ↓	MRE ↓	SR ↑	$MRE_{<0.1}$ ↑
Tumor/Lesion (2K samples)				
MedVision-V0 (7B)	10.5	26.0	100.0	23.5
Lingshu (32B)	35.7	118.6	99.5	4.5
HuatuoGPT-Vision (34B)	44.4	142.4	14.6	0.7
HealthGPT-L14 (14B)	49.9	168.6	100.0	3.3
Llama3.2-Vision (11B)	77.1	248.2	25.3	0.4
MedDr (40B)	97.7	312.7	63.4	0.4
Gemma3 (27B)	226.0	611.8	98.9	0.5
MedGemma (27B)	547.6	1772.6	52.5	0.7
LLava-OneVision (72B)	1016.8	3271.6	100.0	1.4
Qwen2.5-VL (7B)	2933.9	7738.9	95.5	0.7
Qwen2.5-VL (32B)	2721.5	10471.5	16.5	0.2
InternVL3 (38B)	7703.6	23307.5	100.0	0.2
MedGemma (4B)	728794.1	2293400.0	86.0	0.1

4.4 Comparison with a Specialist Model

We compare MedVision-V0 with BiomedParse (Zhao et al., 2025), a text-prompted biomedical foundation model for segmentation across diverse anatomical structures and pathologies. Unlike MedVision-V0, which directly predicts bounding box coordinates and lesion axis lengths end-to-end, BiomedParse produces pixel-level segmentation masks and relies on post-processing to derive the final detection and size estimation results. Bounding box and ellipse fitting are applied to convert BiomedParse's segmentation outputs into the target estimates. As shown in Table 8, MedVision-V0 substantially outperforms BiomedParse on both tasks.

Table 7: Model performance on angle and distance measurement tasks. MRE, $MRE_{<0.1}$, and SR are reported in %. MAEs are given in millimeters (distance) and degrees (angle).

Model	MAE ↓	MRE ↓	SR ↑	$MRE_{<0.1}$ ↑
Ceph-Bio-400, Distance (1000 samples)				
MedVision-V0 (7B)	3.4	5.4	100	85.3
HealthGPT-L14 (14B)	19.5	29.7	95.6	24.1
Lingshu (32B)	214.4	257.6	100	23.5
MedDr (40B)	110.1	175.4	60.4	5.0
MedGemma (27B)	28.8	48.0	33.5	4.7
Qwen2.5-VL (32B)	594.7	1022.1	8.7	0.5
Llama3.2-Vision (11B)	1726.6	2948.5	17.1	0.3
LLaVA-OneVision (72B)	660.4	1084.9	99.9	6.4
Gemma3 (27B)	5563.4	7261.7	98.4	13.5
HuatuoGPT-Vision (34B)	9607.1	18392.7	75.3	4.1
InternVL3 (38B)	14900.1	20754.9	99.7	6.7
MedGemma (4B)	16767.3	27429.4	95.4	0.1
Qwen2.5-VL (7B)	68610.5	101639.4	100	0.5
Ceph-Bio-400, Angle (957 samples)				
MedVision-V0 (7B)	4.7	52.1	99.9	52.0
HealthGPT-L14 (14B)	32.8	727.3	74.9	8.9
Lingshu (32B)	35.0	512.5	100	6.3
MedDr (40B)	47.3	615.8	71.8	5.0
MedGemma (27B)	42.7	971.4	54.8	2.8
Qwen2.5-VL (32B)	33.4	130.5	7.5	0.1
Llama3.2-Vision (11B)	38.9	363.2	93.0	2.9
LLaVA-OneVision (72B)	39.5	530.8	97.3	4.8
Gemma3 (27B)	36.3	702.2	99.9	6.7
HuatuoGPT-Vision (34B)	55.4	1045.9	2.2	0.1
InternVL3 (38B)	31.0	553.0	100	13.7
MedGemma (4B)	35.7	301.1	91.4	6.0
Qwen2.5-VL (7B)	48.0	724.9	97.6	2.0
FeTA24, Distance (100 samples)				
MedVision-V0 (7B)	5.6	15.8	100	42.0
HealthGPT-L14 (14B)	28.6	160.3	70.0	7.0
Lingshu (32B)	43.5	148.4	100	0.0
MedDr (40B)	136.0	599.2	70.0	0.0
MedGemma (27B)	41.5	194.4	43.0	2.0
Qwen2.5-VL (32B)	1255.1	2515.8	31.0	0.0
Llama3.2-Vision (11B)	1198.5	3375.9	28.0	0.0
LLaVA-OneVision (72B)	9167.5	39550.6	100	12.0
Gemma3 (27B)	35.1	173.3	100	9.0
HuatuoGPT-Vision (34B)	111.7	397.8	59.0	1.0
InternVL3 (38B)	8559.1	42057.3	100	11.0
MedGemma (4B)	51.3	135.8	87.0	0.0
Qwen2.5-VL (7B)	13536.3	45568.5	81.0	0.0

5 Conclusion

We introduce **MedVision**, a large-scale, multi-modality, multi-anatomy medical imaging dataset with rich quantitative annotations for detection and measurement tasks. Using MedVision, we establish a comprehensive benchmark to evaluate VLMs on detection, tumor/lesion size estimation, and angle/distance measurement. Our results show that pretrained VLMs perform poorly on these quantitative tasks, whereas supervised and reinforcement fine-tuning (SFT-RFT) with MedVision substantially improves accuracy. Nonetheless, challenges remain, particularly in detecting and measuring small structures and highly variable tumor/lesion targets. We expect MedVision to provide a valuable foundation for advancing quantitative capabilities in medical VLMs. Code and data are publicly available.

Table 8: Comparison with BiomedParse on detection and T/L size estimation.

Detection						
Model	**R** ↑	**P** ↑	**F1** ↑	**IoU** ↑	**SR** ↑	**IoU**$_{>0.5}$ ↑
Anatomy						
MedVision-V0 (7B)	**81.3**	**80.4**	**79.1**	**72.0**	**100.0**	**80.1**
BiomedParse	53.9	57.4	53.8	50.2	64.8	55.3
Tumor/Lesion						
MedVision-V0 (7B)	**52.4**	**50.5**	**46.9**	**38.2**	**100.0**	**40.7**
BiomedParse	33.7	41.0	32.4	27.7	64.8	30.5

T/L Size Estimation				
Model	**MAE** ↓	**MRE** ↓	**SR** ↑	**MRE**$_{<0.1}$ ↑
MedVision-V0 (7B)	**10.5**	**26.0**	**100.0**	23.5
BiomedParse	16.5	52.4	66.4	**36.4**

Limitations

MedVision is currently generalist in terms of being able to do a wide variety of quantitative tasks with a single VLM, without relying on external tools. However, it is specialist in that it is not simultaneously trained to do all the categorical and qualitative description tasks of mainstream or biomedically focused VLMs. Unifying MedVision style quantitative analysis datasets and training recipe with categorical and qualitative datasets and training pipelines remains an important open challenge.

Ethical Considerations. The benchmark reveals that current state-of-the-art VLMs are incapable of accurate medical image detection and measurement. The fine-tuned model MedVision-V0, although demonstrating improved performance, remains far from the accuracy and robustness required for clinical application. Such models must not be used to drive any medical diagnosis or clinical decision-making. Details on intended use of model and data privacy are provided in Appendix J.

References

Felix Ambellan, Alexander Tack, Moritz Ehlke, and Stefan Zachow. 2019. Automated segmentation of knee bone and cartilage combining statistical shape knowledge and convolutional neural networks: Data from the osteoarthritis initiative. *Medical image analysis*, 52:109–118.

Michela Antonelli, Annika Reinke, Spyridon Bakas, Keyvan Farahani, Annette Kopp-Schneider, Bennett A Landman, Geert Litjens, Bjoern Menze, Olaf Ronneberger, Ronald M Summers, and 1 others. 2022. The medical segmentation decathlon. *Nature communications*, 13(1):4128.

Jinze Bai, Shuai Bai, Shusheng Yang, Shijie Wang, Sinan Tan, Peng Wang, Junyang Lin, Chang Zhou, and Jingren Zhou. 2023. Qwen-vl: A versatile vision-language model for understanding, localization, text reading, and beyond. *Preprint*, arXiv:2308.12966.

Shuai Bai, Keqin Chen, Xuejing Liu, Jialin Wang, Wenbin Ge, Sibo Song, Kai Dang, Peng Wang, Shijie Wang, Jun Tang, Humen Zhong, Yuanzhi Zhu, Mingkun Yang, Zhaohai Li, Jianqiang Wan, Pengfei Wang, Wei Ding, Zheren Fu, Yiheng Xu, and 8 others. 2025. Qwen2.5-vl technical report. *Preprint*, arXiv:2502.13923.

Pedro R.A.S. Bassi, Mehmet Can Yavuz, Ibrahim Ethem Hamamci, Sezgin Er, Xiaoxi Chen, Wenxuan Li, Bjoern Menze, Sergio Decherchi, Andrea Cavalli, Kang Wang, Yang Yang, Alan Yuille, and Zongwei Zhou. 2025. Radgpt: Constructing 3d image-text tumor datasets. In *Proceedings of the IEEE/CVF International Conference on Computer Vision (ICCV)*, pages 23720–23730.

Asma Ben Abacha, Sadid A Hasan, Vivek V Datla, Dina Demner-Fushman, and Henning Müller. 2019. Vqa-med: Overview of the medical visual question answering task at imageclef 2019. In *Proceedings of CLEF (Conference and Labs of the Evaluation Forum) 2019 Working Notes*. 9-12 September 2019.

Asma Ben Abacha, Mourad Sarrouti, Dina Demner-Fushman, Sadid A Hasan, and Henning Müller. 2021. Overview of the vqa-med task at imageclef 2021: Visual question answering and generation in the medical domain. In *Proceedings of the CLEF 2021 Conference and Labs of the Evaluation Forum-working notes*. 21-24 September 2021.

Olivier Bernard, Alain Lalande, Clement Zotti, Frederick Cervenansky, Xin Yang, Pheng-Ann Heng, Irem Cetin, Karim Lekadir, Oscar Camara, Miguel Angel Gonzalez Ballester, and 1 others. 2018. Deep learning techniques for automatic mri cardiac multi-structures segmentation and diagnosis: is the problem solved? *IEEE transactions on medical imaging*, 37(11):2514–2525.

Benedikt Boecking, Naoto Usuyama, Shruthi Bannur, Daniel C Castro, Anton Schwaighofer, Stephanie Hyland, Maria Wetscherek, Tristan Naumann, Aditya Nori, Javier Alvarez-Valle, and 1 others. 2022. Making the most of text semantics to improve biomedical vision–language processing. In *European conference on computer vision*, pages 1–21. Springer.

Federico Bolelli, Luca Lumetti, Shankeeth Vinayahalingam, Mattia Di Bartolomeo, Arrigo Pellacani, Kevin Marchesini, Niels Van Nistelrooij, Pieter Van Lierop, Tong Xi, Yusheng Liu, and 1 others. 2024. Segmenting the inferior alveolar canal in cbcts volumes: the toothfairy challenge. *IEEE Transactions on Medical Imaging*.

Federico Bolelli, Kevin Marchesini, Niels van Nistelrooij, Luca Lumetti, Vittorio Pipoli, Elisa Ficarra, Shankeeth Vinayahalingam, and Costantino Grana. 2025. Segmenting maxillofacial structures in cbct volumes. In *Proceedings of the Computer Vision and Pattern Recognition Conference*, pages 5238–5248.

Pierre Chambon, Jean-Benoit Delbrouck, Thomas Sounack, Shih-Cheng Huang, Zhihong Chen, Maya Varma, Steven QH Truong, Chu The Chuong, and Curtis P. Langlotz. 2024. Chexpert plus: Augmenting a large chest x-ray dataset with text radiology reports, patient demographics and additional image formats. *Preprint*, arXiv:2405.19538.

Junying Chen, Chi Gui, Ruyi Ouyang, Anningzhe Gao, Shunian Chen, Guiming Hardy Chen, Xidong Wang, Ruifei Zhang, Zhenyang Cai, Ke Ji, Guangjun Yu, Xiang Wan, and Benyou Wang. 2024. Huatuogpt-vision, towards injecting medical visual knowledge into multimodal llms at scale. *Preprint*, arXiv:2406.19280.

Jack C Cheng, René M Castelein, Winnie C Chu, Aina J Danielsson, Matthew B Dobbs, Theodoros B Grivas, Christina A Gurnett, Keith D Luk, Alain Moreau, Peter O Newton, and 1 others. 2015. Adolescent idiopathic scoliosis. *Nature reviews disease primers*, 1(1):1–21.

Tianzhe Chu, Yuexiang Zhai, Jihan Yang, Shengbang Tong, Saining Xie, Dale Schuurmans, Quoc V. Le, Sergey Levine, and Yi Ma. 2025. Sft memorizes, rl generalizes: A comparative study of foundation model post-training. *Preprint*, arXiv:2501.17161.

Maria Correia de Verdier, Rachit Saluja, Louis Gagnon, Dominic LaBella, Ujjwall Baid, Nourel Hoda Tahon, Martha Foltyn-Dumitru, Jikai Zhang, Maram Alafif, Saif Baig, Ken Chang, Gennaro D'Anna, Lisa Deptula, Diviya Gupta, Muhammad Ammar Haider, Ali Hussain, Michael Iv, Marinos Kontzialis, Paul Manning, and 66 others. 2024. The 2024 brain tumor segmentation (brats) challenge: Glioma segmentation on post-treatment mri. *Preprint*, arXiv:2405.18368.

Arjun D Desai, Andrew M Schmidt, Elka B Rubin, Christopher M Sandino, Marianne S Black, Valentina Mazzoli, Kathryn J Stevens, Robert Boutin, Christopher Ré, Garry E Gold, Brian A Hargreaves, and Akshay S Chaudhari. 2022. Skm-tea: A dataset for accelerated mri reconstruction with dense image labels for quantitative clinical evaluation. *Preprint*, arXiv:2203.06823.

Frank C Detterbeck, Gavitt A Woodard, Anna S Bader, Sanja Dacic, Michael J Grant, Henry S Park, and Lynn T Tanoue. 2024. The proposed ninth edition tnm classification of lung cancer. *Chest*, 166(4):882–895.

Reuben Dorent, Aaron Kujawa, Marina Ivory, Spyridon Bakas, Nicola Rieke, Samuel Joutard, Ben Glocker, Jorge Cardoso, Marc Modat, Kayhan Batmanghelich, Arseniy Belkov, Maria Baldeon Calisto, Jae Won Choi, Benoit M. Dawant, Hexin Dong, Sergio Escalera, Yubo Fan, Lasse Hansen, Mattias P. Heinrich, and 21 others. 2023. Crossmoda 2021 challenge: Benchmark of cross-modality domain adaptation techniques for vestibular schwannoma and cochlea segmentation. *Medical Image Analysis*, 83:102628.

Elizabeth A Eisenhauer, Patrick Therasse, Jan Bogaerts, Lawrence H Schwartz, Danielle Sargent, Robert Ford, Janet Dancey, Stephen Arbuck, Steve Gwyther, Margaret Mooney, and 1 others. 2009. New response evaluation criteria in solid tumours: revised recist guideline (version 1.1). *European journal of cancer*, 45(2):228–247.

Sunan He, Yuxiang Nie, Hongmei Wang, Shu Yang, Yihui Wang, Zhiyuan Cai, Zhixuan Chen, Yingxue Xu, Linshan Wu, Ngai Shing Cheng, and 1 others. 2026. Towards generalizable ai in medicine via generalist–specialist collaboration. *Nature Biomedical Engineering*, pages 1–15.

Xuehai He, Yichen Zhang, Luntian Mou, Eric Xing, and Pengtao Xie. 2020a. Pathvqa: 30000+ questions for medical visual question answering. *Preprint*, arXiv:2003.10286.

Yuting He, Guanyu Yang, Jian Yang, Yang Chen, Youyong Kong, Jiasong Wu, Lijun Tang, Xiaomei Zhu, Jean-Louis Dillenseger, Pengfei Shao, and 1 others. 2020b. Dense biased networks with deep priori anatomy and hard region adaptation: Semi-supervised learning for fine renal artery segmentation. *Medical image analysis*, 63:101722.

Yuting He, Guanyu Yang, Jian Yang, Rongjun Ge, Youyong Kong, Xiaomei Zhu, Shaobo Zhang, Pengfei Shao, Huazhong Shu, Jean-Louis Dillenseger, and 1 others. 2021. Meta grayscale adaptive network for 3d integrated renal structures segmentation. *Medical image analysis*, 71:102055.

Nicholas Heller, Fabian Isensee, Dasha Trofimova, Resha Tejpaul, Zhongchen Zhao, Huai Chen, Lisheng Wang, Alex Golts, Daniel Khapun, Daniel Shats, Yoel Shoshan, Flora Gilboa-Solomon, Yasmeen George, Xi Yang, Jianpeng Zhang, Jing Zhang, Yong Xia, Mengran Wu, Zhiyang Liu, and 26 others. 2023. The kits21 challenge: Automatic segmentation of kidneys, renal tumors, and renal cysts in corticomedullary-phase ct. *Preprint*, arXiv:2307.01984.

Yutao Hu, Tianbin Li, Quanfeng Lu, Wenqi Shao, Junjun He, Yu Qiao, and Ping Luo. 2024. Omnimed-vqa: A new large-scale comprehensive evaluation benchmark for medical lvlm. In *Proceedings of the IEEE/CVF Conference on Computer Vision and Pattern Recognition (CVPR)*, pages 22170–22183.

Jeremy Irvin, Pranav Rajpurkar, Michael Ko, Yifan Yu, Silviana Ciurea-Ilcus, Chris Chute, Henrik Marklund, Behzad Haghgoo, Robyn Ball, Katie Shpanskaya, and 1 others. 2019. Chexpert: A large chest radiograph dataset with uncertainty labels and expert comparison. In *Proceedings of the AAAI conference on artificial intelligence*, volume 33, pages 590–597.

Yuanfeng Ji, Haotian Bai, Chongjian Ge, Jie Yang, Ye Zhu, Ruimao Zhang, Zhen Li, Lingyan Zhanng, Wanling Ma, Xiang Wan, and 1 others. 2022. Amos: A large-scale abdominal multi-organ benchmark for

versatile medical image segmentation. *Advances in neural information processing systems*, 35:36722–36732.

Alistair EW Johnson, Tom J Pollard, Seth J Berkowitz, Nathaniel R Greenbaum, Matthew P Lungren, Chih-ying Deng, Roger G Mark, and Steven Horng. 2019. Mimic-cxr, a de-identified publicly available database of chest radiographs with free-text reports. *Scientific data*, 6(1):317.

Maxime Kayser, Cornelius Emde, Oana-Maria Camburu, Guy Parsons, Bartlomiej Papiez, and Thomas Lukasiewicz. 2022. Explaining chest x-ray pathologies in natural language. In *International Conference on Medical Image Computing and Computer-Assisted Intervention*, pages 701–713. Springer.

Anahita Fathi Kazerooni, Nastaran Khalili, Xinyang Liu, Deep Gandhi, Zhifan Jiang, Syed Muhammed Anwar, Jake Albrecht, Maruf Adewole, Udunna Anazodo, Hannah Anderson, Ujjwal Baid, Timothy Bergquist, Austin J. Borja, Evan Calabrese, Verena Chung, Gian-Marco Conte, Farouk Dako, James Eddy, Ivan Ezhov, and 52 others. 2024. The brain tumor segmentation in pediatrics (brats-peds) challenge: Focus on pediatrics (cbtn-connect-dipgr-asnr-miccai brats-peds). *Preprint*, arXiv:2404.15009.

Dominic LaBella, Valeriia Abramova, Mehdi Astaraki, Andre Ferreira, Zhifan Jiang, Mason C. Cleveland, Ramandeep Kang, Uma M. Lal-Trehan Estrada, Cansu Yalcin, Rachika E. Hamadache, Clara Lisazo, Adrià Casamitjana, Joaquim Salvi, Arnau Oliver, Xavier Lladó, Iuliana Toma-Dasu, Tiago Jesus, Behrus Puladi, Jens Kleesiek, and 86 others. 2025. Analysis of the 2024 brats meningioma radiotherapy planning automated segmentation challenge. *Preprint*, arXiv:2405.18383.

Jason J Lau, Soumya Gayen, Asma Ben Abacha, and Dina Demner-Fushman. 2018. A dataset of clinically generated visual questions and answers about radiology images. *Scientific data*, 5(1):1–10.

Sarah Leclerc, Erik Smistad, Joao Pedrosa, Andreas Østvik, Frederic Cervenansky, Florian Espinosa, Torvald Espeland, Erik Andreas Rye Berg, Pierre-Marc Jodoin, Thomas Grenier, and 1 others. 2019. Deep learning for segmentation using an open large-scale dataset in 2d echocardiography. *IEEE transactions on medical imaging*, 38(9):2198–2210.

Bo Li, Yuanhan Zhang, Dong Guo, Renrui Zhang, Feng Li, Hao Zhang, Kaichen Zhang, Peiyuan Zhang, Yanwei Li, Ziwei Liu, and Chunyuan Li. 2024a. Llava-onevision: Easy visual task transfer. *Preprint*, arXiv:2408.03326.

Chunyuan Li, Cliff Wong, Sheng Zhang, Naoto Usuyama, Haotian Liu, Jianwei Yang, Tristan Naumann, Hoifung Poon, and Jianfeng Gao. 2023. Llava-med: Training a large language-and-vision assistant for biomedicine in one day. *Preprint*, arXiv:2306.00890.

Wenxuan Li, Chongyu Qu, Xiaoxi Chen, Pedro RAS Bassi, Yijia Shi, Yuxiang Lai, Qian Yu, Huimin Xue, Yixiong Chen, Xiaorui Lin, and 1 others. 2024b. Abdomenatlas: A large-scale, detailed-annotated, & multi-center dataset for efficient transfer learning and open algorithmic benchmarking. *Medical Image Analysis*, page 103285.

Tianwei Lin, Wenqiao Zhang, Sijing Li, Yuqian Yuan, Binhe Yu, Haoyuan Li, Wanggui He, Hao Jiang, Mengze Li, Xiaohui Song, Siliang Tang, Jun Xiao, Hui Lin, Yueting Zhuang, and Beng Chin Ooi. 2025. Healthgpt: A medical large vision-language model for unifying comprehension and generation via heterogeneous knowledge adaptation. *Preprint*, arXiv:2502.09838.

Weixiong Lin, Ziheng Zhao, Xiaoman Zhang, Chaoyi Wu, Ya Zhang, Yanfeng Wang, and Weidi Xie. 2023. Pmc-clip: Contrastive language-image pre-training using biomedical documents. *Preprint*, arXiv:2303.07240.

Claudia Lindner, Ching-Wei Wang, Cheng-Ta Huang, Chung-Hsing Li, Sheng-Wei Chang, and Tim F Cootes. 2016. Fully automatic system for accurate localisation and analysis of cephalometric landmarks in lateral cephalograms. *Scientific reports*, 6(1):33581.

Bo Liu, Li-Ming Zhan, Li Xu, Lin Ma, Yan Yang, and Xiao-Ming Wu. 2021. Slake: A semantically-labeled knowledge-enhanced dataset for medical visual question answering. *Preprint*, arXiv:2102.09542.

Haotian Liu, Chunyuan Li, Qingyang Wu, and Yong Jae Lee. 2023. Visual instruction tuning. *Advances in neural information processing systems*, 36:34892–34916.

Luca Lumetti, Vittorio Pipoli, Federico Bolelli, Elisa Ficarra, and Costantino Grana. 2024. Enhancing patch-based learning for the segmentation of the mandibular canal. *IEEE Access*, 12:79014–79024.

Jun Ma, Yao Zhang, Song Gu, Cheng Ge, Shihao Mae, Adamo Young, Cheng Zhu, Xin Yang, Kangkang Meng, Ziyan Huang, Fan Zhang, Yuanke Pan, Shoujin Huang, Jiacheng Wang, Mingze Sun, Rongguo Zhang, Dengqiang Jia, Jae Won Choi, Natália Alves, and 18 others. 2024. Unleashing the strengths of unlabelled data in deep learning-assisted pan-cancer abdominal organ quantification: the flare22 challenge. *The Lancet Digital Health*, 6(11):e815–e826.

Jun Ma, Yao Zhang, Song Gu, Cheng Zhu, Cheng Ge, Yichi Zhang, Xingle An, Congcong Wang, Qiyuan Wang, Xin Liu, Shucheng Cao, Qi Zhang, Shangqing Liu, Yunpeng Wang, Yuhui Li, Jian He, and Xiaoping Yang. 2022. Abdomenct-1k: Is abdominal organ segmentation a solved problem? *IEEE Transactions on Pattern Analysis and Machine Intelligence*, 44(10):6695–6714.

Jiazhen Pan, Che Liu, Junde Wu, Fenglin Liu, Jiayuan Zhu, Hongwei Bran Li, Chen Chen, Cheng Ouyang,

and Daniel Rueckert. 2025. Medvlm-r1: Incentivizing medical reasoning capability of vision-language models (vlms) via reinforcement learning. *Preprint*, arXiv:2502.19634.

Kelly Payette, Hongwei Bran Li, Priscille De Dumast, Roxane Licandro, Hui Ji, Md Mahfuzur Rahman Siddiquee, Daguang Xu, Andriy Myronenko, Hao Liu, Yuchen Pei, and 1 others. 2023. Fetal brain tissue annotation and segmentation challenge results. *Medical image analysis*, 88:102833.

Andrew Sellergren, Sahar Kazemzadeh, Tiam Jaroensri, Atilla Kiraly, Madeleine Traverse, Timo Kohlberger, Shawn Xu, Fayaz Jamil, Cían Hughes, Charles Lau, Justin Chen, Fereshteh Mahvar, Liron Yatziv, Tiffany Chen, Bram Sterling, Stefanie Anna Baby, Susanna Maria Baby, Jeremy Lai, Samuel Schmidgall, and 62 others. 2025. Medgemma technical report. *Preprint*, arXiv:2507.05201.

Pengfei Shao, Chao Qin, Changjun Yin, Xiaoxin Meng, Xiaobing Ju, Jie Li, Qiang Lv, Wei Zhang, and Zhengquan Xu. 2011. Laparoscopic partial nephrectomy with segmental renal artery clamping: technique and clinical outcomes. *European urology*, 59(5):849–855.

Pengfei Shao, Lijun Tang, Pu Li, Yi Xu, Chao Qin, Qiang Cao, Xiaobing Ju, Xiaoxin Meng, Qiang Lv, Jie Li, and 1 others. 2012. Precise segmental renal artery clamping under the guidance of dual-source computed tomography angiography during laparoscopic partial nephrectomy. *European urology*, 62(6):1001–1008.

Zhihong Shao, Peiyi Wang, Qihao Zhu, Runxin Xu, Junxiao Song, Xiao Bi, Haowei Zhang, Mingchuan Zhang, Y. K. Li, Y. Wu, and Daya Guo. 2024. Deepseekmath: Pushing the limits of mathematical reasoning in open language models. *Preprint*, arXiv:2402.03300.

Guangming Sheng, Chi Zhang, Zilingfeng Ye, Xibin Wu, Wang Zhang, Ru Zhang, Yanghua Peng, Haibin Lin, and Chuan Wu. 2025. Hybridflow: A flexible and efficient rlhf framework. In *Proceedings of the Twentieth European Conference on Computer Systems*, EuroSys '25, page 1279–1297. ACM.

Sanjay Subramanian, Lucy Lu Wang, Ben Bogin, Sachin Mehta, Madeleine van Zuylen, Sravanthi Parasa, Sameer Singh, Matt Gardner, and Hannaneh Hajishirzi. 2020. MedICaT: A dataset of medical images, captions, and textual references. In *Findings of the Association for Computational Linguistics: EMNLP 2020*, pages 2112–2120, Online. Association for Computational Linguistics.

Gemma Team, Aishwarya Kamath, Johan Ferret, Shreya Pathak, Nino Vieillard, Ramona Merhej, Sarah Perrin, Tatiana Matejovicova, Alexandre Ramé, Morgane Rivière, Louis Rouillard, Thomas Mesnard, Geoffrey Cideron, Jean bastien Grill, Sabela Ramos, Edouard Yvinec, Michelle Casbon, Etienne Pot, Ivo Penchev, and 197 others. 2025a. Gemma 3 technical report. *Preprint*, arXiv:2503.19786.

LASA Team, Weiwen Xu, Hou Pong Chan, Long Li, Mahani Aljunied, Ruifeng Yuan, Jianyu Wang, Chenghao Xiao, Guizhen Chen, Chaoqun Liu, Zhaodonghui Li, Yu Sun, Junao Shen, Chaojun Wang, Jie Tan, Deli Zhao, Tingyang Xu, Hao Zhang, and Yu Rong. 2025b. Lingshu: A generalist foundation model for unified multimodal medical understanding and reasoning. *Preprint*, arXiv:2506.07044.

Jakob Wasserthal, Hanns-Christian Breit, Manfred T Meyer, Maurice Pradella, Daniel Hinck, Alexander W Sauter, Tobias Heye, Daniel T Boll, Joshy Cyriac, Shan Yang, and 1 others. 2023. Totalsegmentator: robust segmentation of 104 anatomic structures in ct images. *Radiology: Artificial Intelligence*, 5(5):e230024.

Chaoyi Wu, Xiaoman Zhang, Ya Zhang, Hui Hui, Yanfeng Wang, and Weidi Xie. 2025. Towards generalist foundation model for radiology by leveraging web-scale 2d&3d medical data. *Nature Communications*, 16(1):7866.

Kaiyuan Yang, Fabio Musio, Yihui Ma, Norman Juchler, Johannes C. Paetzold, Rami Al-Maskari, Luciano Höher, Hongwei Bran Li, Ibrahim Ethem Hamamci, Anjany Sekuboyina, Suprosanna Shit, Houjing Huang, Chinmay Prabhakar, Ezequiel de la Rosa, Bastian Wittmann, Diana Waldmannstetter, Florian Kofler, Fernando Navarro, Martin Menten, and 94 others. 2025. Benchmarking the cow with the topcow challenge: Topology-aware anatomical segmentation of the circle of willis for cta and mra. *Preprint*, arXiv:2312.17670.

Yongcheng Yao and Weitian Chen. 2025. Quantifying knee cartilage shape and lesion: From image to metrics. In *Applications of Medical Artificial Intelligence*, pages 162–172, Cham. Springer Nature Switzerland.

Yongcheng Yao, Junru Zhong, Liping Zhang, Sheheryar Khan, and Weitian Chen. 2024. Cartimorph: A framework for automated knee articular cartilage morphometrics. *Medical Image Analysis*, 91:103035.

Jin Ye, Guoan Wang, Yanjun Li, Zhongying Deng, Wei Li, Tianbin Li, Haodong Duan, Ziyan Huang, Yanzhou Su, Benyou Wang, and 1 others. 2024. Gmai-mmbench: A comprehensive multimodal evaluation benchmark towards general medical ai. *Advances in Neural Information Processing Systems*, 37:94327–94427.

Theodore Zhao, Yu Gu, Jianwei Yang, Naoto Usuyama, Ho Hin Lee, Sid Kiblawi, Tristan Naumann, Jianfeng Gao, Angela Crabtree, Jacob Abel, and 1 others. 2025. A foundation model for joint segmentation, detection and recognition of biomedical objects across nine modalities. *Nature methods*, 22(1):166–176.

Tianhong Zhou, Yin Xu, Yingtao Zhu, Chuxi Xiao, Haiyang Bian, Lei Wei, and Xuegong Zhang. 2025.

Drvd-bench: Do vision-language models reason like human doctors in medical image diagnosis? *Preprint*, arXiv:2505.24173.

Jinguo Zhu, Weiyun Wang, Zhe Chen, Zhaoyang Liu, Shenglong Ye, Lixin Gu, Hao Tian, Yuchen Duan, Weijie Su, Jie Shao, Zhangwei Gao, Erfei Cui, Xuehui Wang, Yue Cao, Yangzhou Liu, Xingguang Wei, Hongjie Zhang, Haomin Wang, Weiye Xu, and 32 others. 2025. Internvl3: Exploring advanced training and test-time recipes for open-source multimodal models. *Preprint*, arXiv:2504.10479.

Yongshuo Zong, Oisin Mac Aodha, and Timothy M. Hospedales. 2024. Self-supervised multimodal learning: A survey. *IEEE Transactions on Pattern Analysis and Machine Intelligence*.

A Dataset and Benchmark Comparison

Early medical image–text dataset construction mainly targeted visual question answering (VQA), including VQA-RAD (Lau et al., 2018), VQA-Med (Ben Abacha et al., 2019, 2021), SLAKE (Liu et al., 2021), and PathVQA (He et al., 2020a). These resources support structured evaluation of medical image understanding via question–answer pairs, but the evaluations remain predominantly categorical. Large-scale image-text corpora such as Chexpert (Irvin et al., 2019), Chexpert Plus (Chambon et al., 2024), MIMIC-CXR (Johnson et al., 2019), MIMIC-NLE (Kayser et al., 2022), MS-CXR (Boecking et al., 2022), and PMC-OA (Lin et al., 2023) further support the development of VLMs by aligning medical images with clinical reports or natural language explanations from experts. A comparison of existing medical image–text datasets is summarized in Table 9. Notably, these datasets lack quantitative annotations, limiting their utility for evaluating models on measurement tasks.

Building on these resources, recent VLMs have been adapted to the medical domain, including LLaVA-Med (Li et al., 2023), MedDr (He et al., 2026), HuatuoGPT-Vision (Chen et al., 2024), HealthGPT-L14 (14B) (Lin et al., 2025), MedGemma (Sellergren et al., 2025), Lingshu (Team et al., 2025b), and MedVLM-R1 (Pan et al., 2025). Several recent works have aimed to systematically evaluate medical VLMs, including GMAI-MMBench (Ye et al., 2024), OmniMed-VQA (Hu et al., 2024), RadBench (Wu et al., 2025), and DrVD-Bench (Zhou et al., 2025). These benchmarks emphasize descriptive or categorical tasks such as image understanding and report generation, with limited evaluation of quantitative measurement abilities.

Table 9: Comparison of medical datasets. XR: X-ray; MR: Magnetic Resonance Imaging; CT: Computed Tomography; PET: positron emission tomography; US: Ultrasound.

Dataset	Size	Anatomy	Modality	Quantitative
VQA-RAD	3.5K	multiple	XR, CT, MR	✗
VQA-Med	5K	multiple	XR, CT, MR, US, PET	✗
SLAKE	14K	multiple	XR, CT, MR	✗
PathVQA	33K	N/A	pathology	✗
Chexpert	224K	chest	XR	✗
Chexpert Plus	223K	chest	XR	✗
MIMIC-CXR	377K	chest	XR	✗
MIMIC-NLE	38K	chest	XR	✗
MS-CXR	1.2K	chest	XR	✗
PMC-OA	1.6M	multiple	diverse	✗
MedVision	30.8M	multiple	XR, CT, MR, US, PET	✓

B Dataset Examples

Figure 6 shows preprocessed images of each dataset and examples of three types of quantitative annotations.

C Full Dataset Statistics

Table 10 provides the full statistics of the MedVision dataset, including the number of samples for each annotation type (bounding box, tumor/lesion size, and angle/distance) across all included datasets. This detailed breakdown highlights the diversity and scale of the dataset, which supports comprehensive evaluation of VLMs on a wide range of quantitative medical imaging tasks.

D VLMs Version

Table 11 lists the HuggingFace model IDs of the evaluated open-weight VLMs.

E VLM Image Processing Strategy

Different VLMs define their own image processing strategy in the image processor classes (or equivalent modules), where image processing pipelines including resizing, cropping, padding, and rescaling are defined. We summarized the image resizing strategies of the evaluated VLMs in Table 12, upon which we designed appropriate pixel size adjustment for conveying physical spacing information to VLMs.

F Metric Definition

Success Rate (SR). For all tasks, success rate is defined as the proportion of model responses where

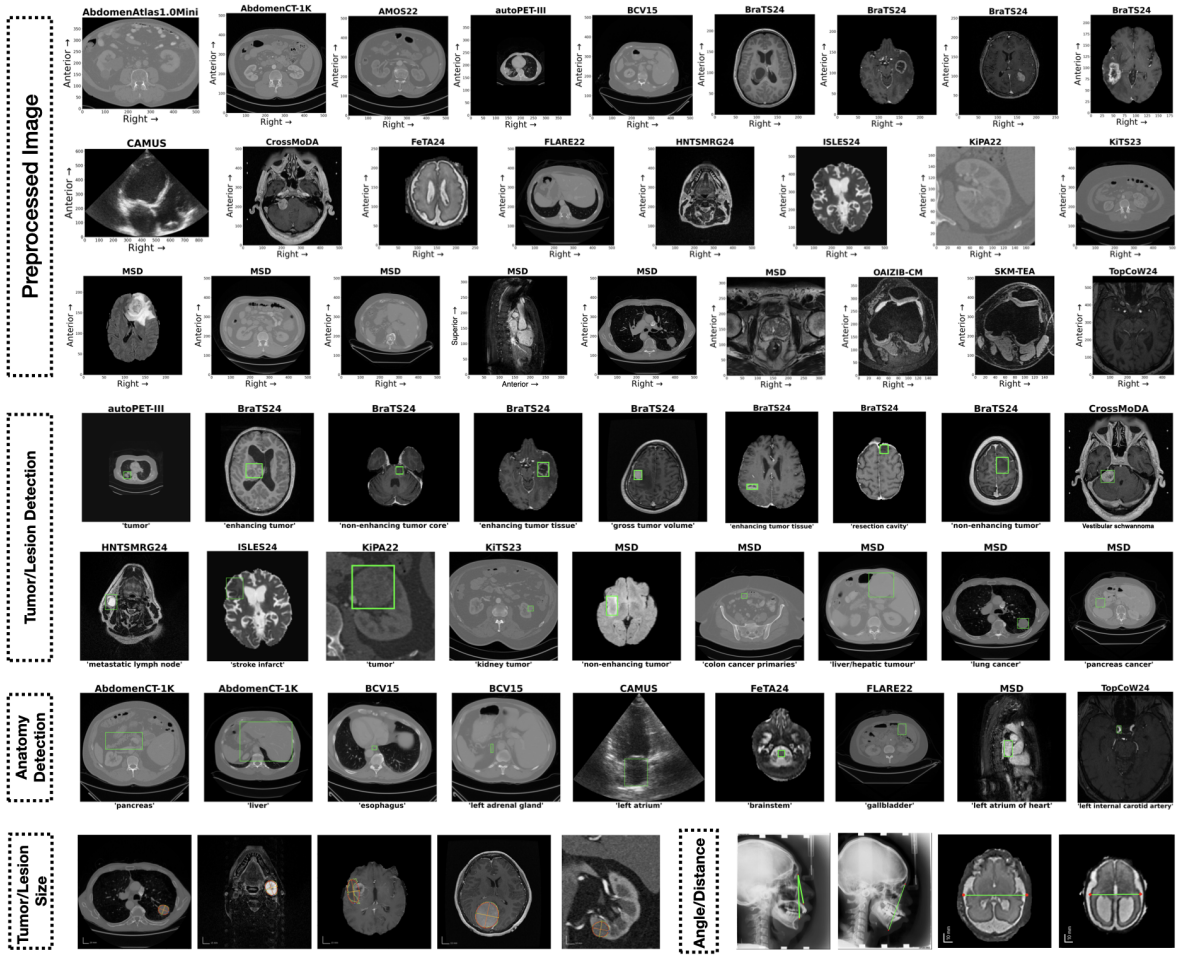


Figure 6: Preprocessed images and annotations from MedVision dataset.

the required numeric values can be parsed. SR indicates model's instruction-following ability.

Detection Metrics. For detection tasks, we calculated precision (P), recall (R), F1 score, and intersection over union (IoU) from the true positive (TP), false positive (FP), and false negative (FN) area. Given a ground truth bounding box B_y and a predicted bounding box B_x, the TP, FP, and FN areas are defined as follows:

$$\text{TP} = \text{area}(B_x \cap B_y), \tag{1}$$
$$\text{FP} = \text{area}(B_x - \text{TP}), \tag{2}$$
$$\text{FN} = \text{area}(B_y - \text{TP}). \tag{3}$$

Precision, recall, F1 score, and IoU are then calculated as:

$$\text{Precision} = \frac{\text{TP}}{\text{TP} + \text{FP}}, \tag{4}$$
$$\text{Recall} = \frac{\text{TP}}{\text{TP} + \text{FN}}, \tag{5}$$
$$\text{F1} = \frac{2 \cdot \text{TP}}{2 \cdot \text{TP} + \text{FP} + \text{FN}}, \tag{6}$$
$$\text{IoU} = \frac{\text{TP}}{\text{TP} + \text{FP} + \text{FN}}, \tag{7}$$

where the region-based F1 score is termed as Dice Similarity Coefficient (DSC) in image segmentation literature.

Measurement Metrics. For the tumor/lesion size and angle/distance measurement tasks, we calculated the mean absolute error (MAE) and mean relative error (MRE) between predictions $\mathbf{x}^{(n)}$ and

Table 10: Full statistics of the MedVision dataset. MRI: Magnetic Resonance Imaging; CT: Computed Tomography; PET: positron emission tomography; US: Ultrasound; b-box: bounding box; T/L: tumor/lesion size; A/D: angle/distance; HF: HuggingFace; GC: Grand-Challenge; † redistributed.

Dataset	Anatomy	Modality	Annotation	Availability	Source	# Sample (Train / Test)		
						b-box	T/L	A/D
AbdomenAtlas	abdomen	CT	b-box	open	HF	6.8 / 2.9M	0	0
AbdomenCT-1K	abdomen	CT	b-box	open	Zenodo	0.7 / 0.3M	0	0
ACDC	heart	MRI	b-box	open	HF†, others	9.5 / 4.8K	0	0
AMOS22	abdomen	CT, MRI	b-box	open	Zenodo	0.8 / 0.3M	0	0
autoPET-III	whole body	CT, PET	b-box, T/L	open	HF†, others	22 / 9.7K	0.5 / 0.2K	0
BCV15	abdomen	CT	b-box	open	HF†, Synapse	71 / 30K	0	0
BraTS24	brain	MRI	b-box, T/L	open	HF†, Synapse	0.8 / 0.3M	7.9 / 3.1K	0
CAMUS	heart	US	b-box	open	HF†, others	0.7 / 0.3M	0	0
Ceph-Bio-400	head and neck	X-ray	b-box, A/D	open	HF†, others	0	0	5.3 / 2.3K
CrossModDA	brain	MRI	b-box	open	HF†, Zenodo	3.0 / 1.0K	0	0
FeTA24	fetal brain	MRI	b-box, A/D	registration	Synapse	34 / 15K	0	0.2 / 0.1K
FLARE22	abdomen	CT	b-box	open	HF†, others	72 / 33K	0	0
HNTSMRG24	head and neck	MRI	b-box, T/L	open	Zenodo	18 / 6.6K	1.0 / 0.4K	0
ISLES24	brain	MRI	b-box	open	HF†, GC	7.3 / 2.5K	0	0
KiPA22	kidney	CT	b-box, T/L	open	HF†, GC	26 / 11K	2.1 / 1.0K	0
KiTS23	kidney	CT	b-box, T/L	open	HF†, GC	80 / 35K	5.9 / 2.6K	0
MSD	multiple	CT, MRI	b-box, T/L	open	others	0.2 / 0.1M	5.3 / 2.2K	0
OAIZIB-CM	knee	MRI	b-box	open	HF	0.5 / 0.2M	0	0
SKM-TEA	knee	MRI	b-box	registration	others	0.2 / 0.1M	0	0
ToothFairy2	tooth	CT	b-box	registration	others	1.0 / 0.4M	0	0
TopCoW24	brain	CT, MRI	b-box	open	HF†, Zenodo	43 / 20K	0	0
TotalSegmentator	multiple	CT, MRI	b-box	open	HF†, Zenodo	9.6 / 4.0M	0	0
Total						**22 / 9.2M**	**23 / 9.6K**	**5.6 / 2.4K**

Table 11: HuggingFace model ID of the evaluated open-weight VLMs.

Model	HuggingFace Model ID
Qwen2.5-VL (7B)	`Qwen/Qwen2.5-VL-7B-Instruct`
Qwen2.5-VL (32B)	`Qwen/Qwen2.5-VL-32B-Instruct`
Lingshu (32B)	`lingshu-medical-mllm/Lingshu-32B`
InternVL3 (38B)	`OpenGVLab/InternVL3-38B`
Gemma3 (27B)	`google/gemma-3-27b-it`
MedGemma (4B)	`google/medgemma-4b-it`
MedGemma (27B)	`google/medgemma-27b-it`
Llama3.2-Vision (11B)	`meta-llama/Llama-3.2-11B-Vision-Instruct`
LLava-OneVision (72B)	`llava-hf/llava-onevision-qwen2-72b-ov-hf`
MedDr (40B)	`Sunanhe/MedDr_0401`
HuatuoGPT-Vision (34B)	`FreedomIntelligence/HuatuoGPT-Vision-34B`
HealthGPT-L14 (14B)	`lintw/HealthGPT-L14`

ground truths $\mathbf{y}^{(n)}$ as follows:

$$\text{MAE} = \frac{1}{N}\sum_{i=1}^{N}\frac{1}{n}\sum_{j=1}^{n}|x_i^j - y_i^j|, \tag{8}$$

$$\text{MRE} = \frac{1}{N}\sum_{i=1}^{N}\frac{1}{n}\sum_{j=1}^{n}(|x_i^j - y_i^j|/y_i^j), \tag{9}$$

where N is the total number of samples, and n is the number of values to be measured in each sample. For tumor/lesion size measurement, $n = 2$ (major and minor axis lengths). For angle/distance measurement, $n = 1$.

Since the detection and measurement metrics are calculated only on the successfully parsed predictions, indicating the model prediction accuracy, we also report metrics that reflect both the instruction-following ability and prediction accuracy:

$$\text{MRE}_{<k} = \frac{1}{N}\sum_{i=1}^{N}\mathbb{I}(k - \frac{1}{n}\sum_{j=1}^{n}|x_i^j - y_i^j|/y_i^j), \tag{10}$$

where $\mathbb{I}(x)$ is the step function that returns 1 for $x \geq 0$. $\text{MRE}_{<k}$ indicates the proportion of samples with relative error less than k. Similarly, $\text{IoU}_{>k}$ indicates the proportion of samples with IoU greater than k, defined as:

$$\text{IoU}_{>k} = \frac{1}{N}\sum_{i=1}^{N}\mathbb{I}(\text{IoU}_i - k). \tag{11}$$

G Computational Resources & Software

Computational Resources. Model evaluation used 4 NVIDIA H100 (80 GB) GPUs; training of

Table 12: Image resize strategies of VLMs. ‡ aspect ratio preserved

Model	Image Size	Image Resize Strategy
Qwen2.5-VL (7B, 32B)	dynamic	reshape to a size divisible by 28x28 patch
Lingshu (32B)	dynamic	reshape to a size divisible by 28x28 patch
InternVL3 (38B)	448x448	reshape to a fixed size
Gemma3 (27B)	896x896	reshape to a fixed size
MedGemma (4B, 27B)	896x896	reshape to a fixed size
Llama3.2-Vision (11B)	dynamic	reshape‡ to fit in a tiled canvas (patch size: 560x560)
LLava-OneVision (72B)	dynamic	reshape‡ to fit in a tiled canvas (patch size: 384x384)
MedDr (40B)	448x448	reshape to a fixed size
HuatuoGPT-Vision (34B)	336x336	reshape to a fixed size
HealthGPT-L14 (14B)	336x336	reshape to a fixed size

MedVision-V0 used 4 NVIDIA H200 (140 GB) GPUs.

Software. We developed and release two codebases: `medvision_bm` (v1.1.0) for benchmarking and `medvision_ds` (v1.1.0) for dataset access. Because different VLMs require different dependency versions, a per-model requirements file is provided for each evaluated model. A dedicated environment specification is also provided for model fine-tuning. Reinforcement fine-tuning (RFT) was performed using verl v0.7.0. Code for dataset construction, benchmarking, and fine-tuning are publicly available.

H MedVision-V0 Overview

Qualitative Results. Figure 7 shows random samples of MedVision-V0 responses for the detection task. For the A/D task, Figure 8 shows random response samples, while Figures 9 and 10 illustrate individual examples for angle and distance measurement, respectively.

Quantitative Results. Figure 11 summarizes the performance gains from each training stage (base → SFT → SFT-RFT): the average performance metric in each label group is presented for the base, SFT, and SFT-RFT model, and the distribution of metric values in each group for the SFT-RFT model is visualized as a violin plot. Table 13 reports the full quantitative ablation across all three tasks, and Table 14 presents out-of-distribution generalization results. We evaluate two OOD settings: **Plane-OOD**, where test samples involve imaging planes not seen during training for a given anatomical target (e.g., a structure trained on axial CT slices evaluated on coronal or sagittal views); and **Target-OOD**, where test samples involve anatomical targets (structures or tumors) entirely absent from the training label set. Across both OOD settings, SFT-RFT consistently outperforms the SFT model, indicating that reinforcement learning fosters stronger generalization beyond memorized training distributions. This observation is consistent with the finding that RL generalizes better than SFT (Chu et al., 2025).

Table 13: Training progression of MedVision-V0: base (Qwen2.5-VL-7B) → SFT → SFT-RFT (MedVision-V0) across all three tasks.

Detection						
Model	**R↑**	**P↑**	**F1↑**	**IoU↑**	**SR↑**	**IoU$_{>.5}$↑**
Anatomy (18 regions, 13.4K samples)						
base	69.6	12.2	16.7	11.3	99.3	5.6
SFT	79.8	80.5	78.3	71.2	100	79.3
SFT-RFT	81.3	80.4	79.1	72.0	100	80.1
Tumor/Lesion (8 regions, 8.5K samples)						
base	77.4	3.8	6.5	3.6	99.6	0.0
SFT	47.9	49.3	44.1	35.4	100	37.0
SFT-RFT	52.4	50.5	46.9	38.2	100	40.7

Tumor/Lesion Size Estimation				
Model	**MAE↓**	**MRE↓**	**SR↑**	**MRE$_{<0.1}$↑**
Tumor/Lesion Size (2K samples)				
base	2933.9	7738.9	95.5	0.7
SFT	11.3	28.6	100	20.6
SFT-RFT	10.5	26.0	100	23.5

Angle/Distance Measurement				
Model	**MAE↓**	**MRE↓**	**SR↑**	**MRE$_{<0.1}$↑**
Ceph-Dist. (1K samples)				
base	68610.5	101639.4	100	0.5
SFT	4.1	6.4	100	82.0
SFT-RFT	3.4	5.4	100	85.3
Ceph-Angle (957 samples)				
base	48.0	724.9	97.6	2.0
SFT	5.8	53.3	100	48.8
SFT-RFT	4.7	52.1	99.9	52.0
FeTA-Dist. (100 samples)				
base	13536.3	45568.5	81.0	0.0
SFT	5.6	18.2	100	35.0
SFT-RFT	5.6	15.8	100	42.0

I Details of Detection Performance

I.1 Label Level Detection Performance

Figure 12 shows the label level detection performance of VLMs at each box-image-ratio group. Box-image-ratio is defined as the area ratio of the bounding box to the image. Labels are grouped into different box-image-ratio ranges. We visualized the composition of box-image-ratio groups for

Table 14: OOD generalization of SFT and SFT-RFT (MedVision-V0) on detection and T/L size estimation tasks.

Detection: Plane-OOD						
Model	**R↑**	**P↑**	**F1↑**	**IoU↑**	**SR↑**	**IoU$_{>.5}$↑**
Anatomy (25 regions, 25.6K samples)						
SFT	48.5	55.7	49.0	43.7	100	47.4
SFT-RFT	49.3	54.7	49.5	44.3	100	47.5
Tumor/Lesion (16 regions, 15.2K samples)						
SFT	30.1	43.8	30.7	23.9	100	22.9
SFT-RFT	35.7	48.8	36.6	28.9	100	28.1
Detection: Target-OOD						
Model	**R↑**	**P↑**	**F1↑**	**IoU↑**	**SR↑**	**IoU$_{>.5}$↑**
Anatomy (27 regions, 5.6K samples)						
SFT	31.3	44.6	32.8	28.4	98.5	29.4
SFT-RFT	34.8	46.9	36.0	31.2	98.6	31.6
Tumor/Lesion (3 regions, 7.3K samples)						
SFT	40.6	50.0	40.2	32.7	99.8	35.4
SFT-RFT	47.4	51.5	45.5	38.0	99.9	41.7

T/L Size: Plane-OOD (14 labels, 4K samples)				
Model	**MAE↓**	**MRE↓**	**SR↑**	**MRE$_{<0.1}$↑**
SFT	23.7	41.7	100	5.8
SFT-RFT	21.3	36.3	100	7.5
T/L Size: Target-OOD (5 labels, 300 samples)				
Model	**MAE↓**	**MRE↓**	**SR↑**	**MRE$_{<0.1}$↑**
SFT	12.0	36.2	100	12.8
SFT-RFT	10.9	31.7	100	17.1

each label at the bottom of Figure 12. For each box-image-ratio group and label combination, we visualized recall, precision, and F1 score. Figure 12 is a detailed map of VLM performance at various target sizes and labels.

I.2 Effect of Target Size

Figure 12 shows a trend of increasing detection performance with larger target sizes (box-image-ratio). To further illustrate this effect, we grouped all detection targets into different box-image-ratio groups, and calculated the overall detection performance for each group. As shown in Figure 13, precision and recall is positively correlated to relative target size (box-image-ratio). Our fine-tuned model, **MedVision-V0**, consistently outperforms all off-the-shelf models across all target sizes.

J Intended Use and Data Privacy

Intended Use. MedVision is released under the Creative Commons Attribution 4.0 International (CC-BY 4.0) license. Users are permitted to utilize, adapt, and build upon this dataset for both academic and commercial purposes, provided that appropriate credit is given. Users are reminded that MedVision acts as a meta-dataset built upon various publicly available source datasets. While the annotations provided by MedVision are covered by the CC-BY 4.0 license, any downstream application must continue to comply with the specific usage terms and licensing requirements stipulated by the curators of the original raw imaging data. It is the responsibility of the user to ensure that their application of this data aligns with the license agreements of all constituent source datasets.

Data Privacy. All source imaging datasets incorporated in MedVision were publicly released in anonymized form by their respective curators. The annotations contributed by MedVision (bounding boxes, tumor/lesion size measurements, and angle/distance measurements) are purely geometric descriptors of image content and contain no information that could identify individual subjects.

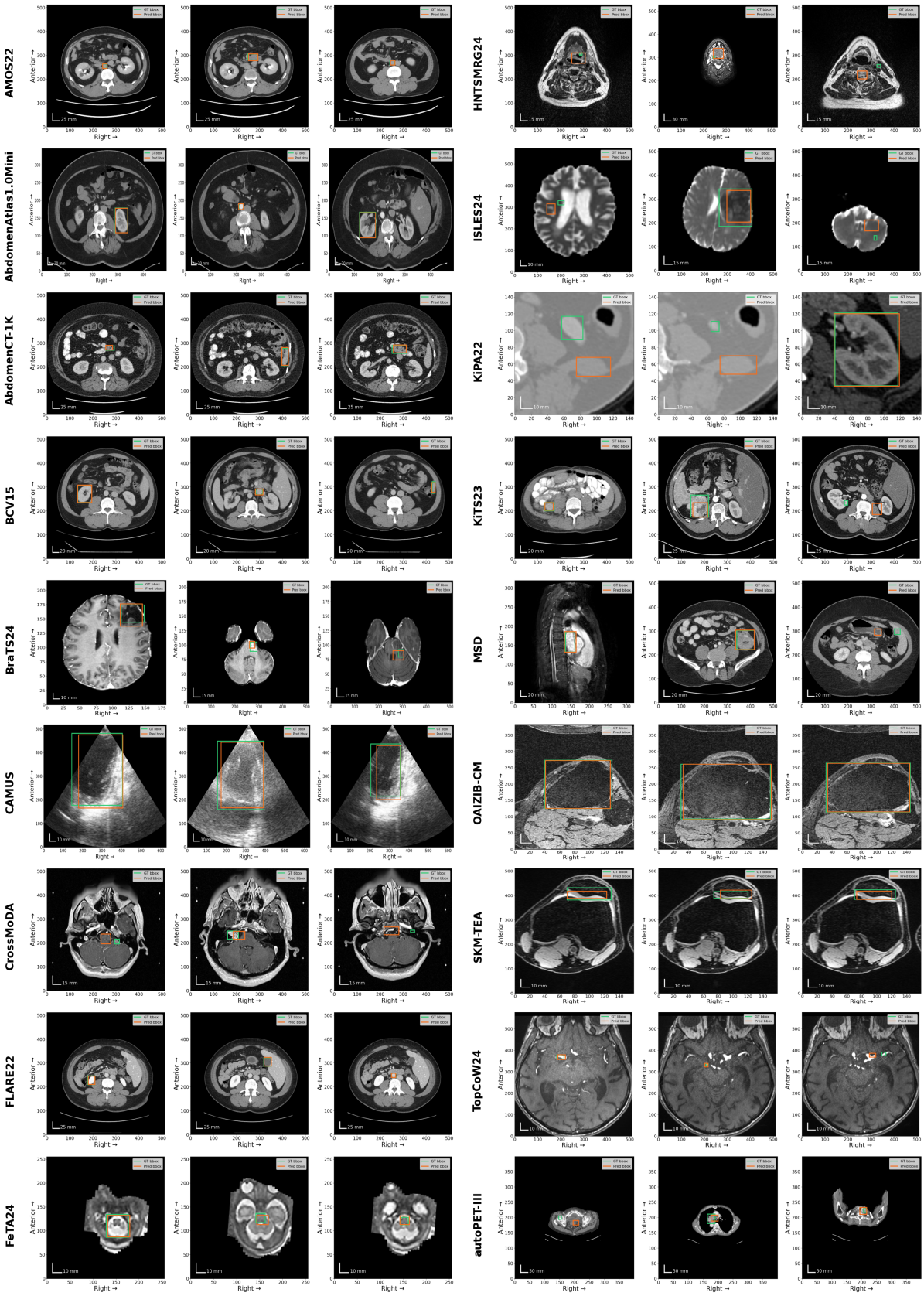


Figure 7: Random samples of model responses in the detection task.

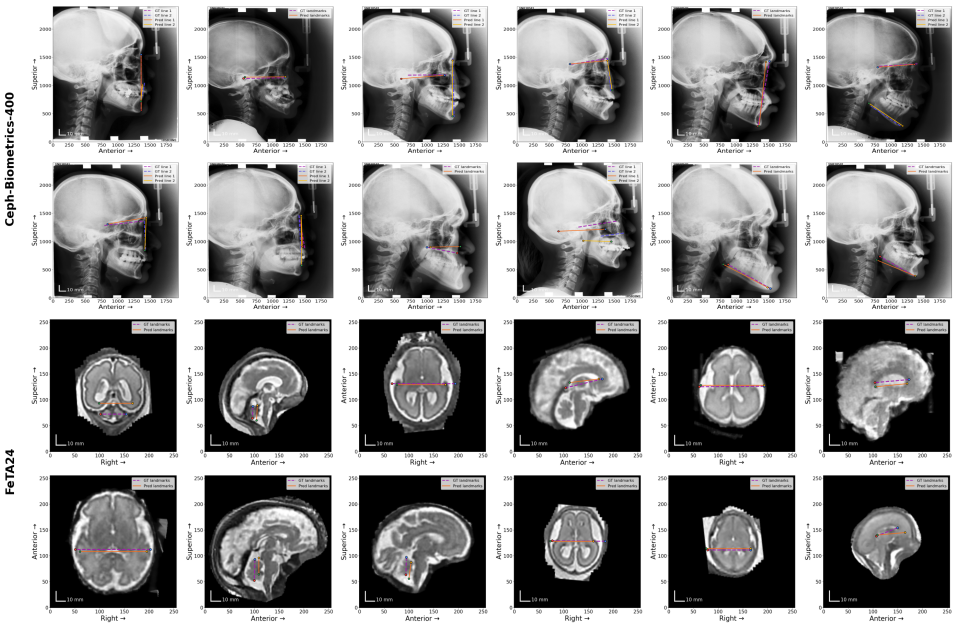


Figure 8: Random samples of model responses in the A/D task.

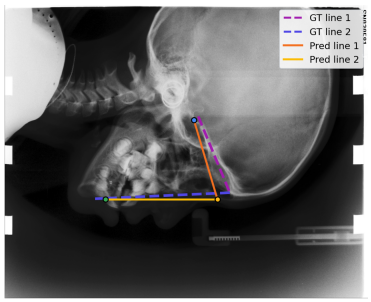
[Prompt]

Task:
Given the input medical image: **cephalogram (head and neck X-ray)**, estimate the angle between 2 lines in degree: (line 1) **the line connecting sella and nasion**, (line 2) **the line connecting nasion and supramentale**.
Additional information:
The image size is **504** pixels (width) x **504** pixels (height).
The pixel size for this image is **0.476** mm (width) x **0.384** mm (height).
Format requirement:
The final answer must be enclosed within <answer> </answer> tags. The answer should be a single decimal number without units or extra text.
Reasoning steps:
Step 1: Identify line 1 and record the relative coordinates of its two endpoints in the format (x, y) = (relative position in width direction, relative position in height direction). Denote the endpoints as (x1_line1, y1_line1) and (x2_line1, y2_line1). Step 2: Identify line 2 and record the relative coordinates of its two endpoints in the same (x, y) format. Denote them as (x1_line2, y1_line2) and (x2_line2, y2_line2). Step 3: Given the pixel dimensions (pixel_width, pixel_height) and image size (image_width, image_height), compute the angle between the two lines using the formula: angle = arccos(|A · B| / (||A|| ||B||), where A and B are the vectors of the two lines computed from the physical coordinates of their endpoints. A = ((x2_line1 - x1_line1) * image_width * pixel_width, (y2_line1 - y1_line1) * image_height * pixel_height) and B = ((x2_line2 - x1_line2) * image_width * pixel_width, (y2_line2 - y1_line2) * image_height * pixel_height). Denote A=(Ax, Ay) and B=(Bx, By). Then, angle = arccos(|Ax*Bx + Ay*By| / (sqrt(Ax^2 + Ay^2) * sqrt(Bx^2 + By^2))). Report the reasoning process and final answer within <think> </think> and <answer> </answer> tags, respectively. Inside <think> </think>, include reasoning and step results using <step-k-reasoning> </step-k-reasoning> and <step-k-answer> </step-k-answer> tags.
Follow the reasoning steps to get the final answer in the required format.



[Response]

<think> <step-1-reasoning> I need to identify the relative coordinates of sella and nasion that define line 1. The relative coordinates must be written as (x1_line1, y1_line1), (x2_line1, y2_line1), where x is the relative position in width and y is the relative position in height. I understand that the origin of the coordinate system is at the lower-left corner of the image.
</step-1-reasoning> <step-1-answer> The relative coordinates of sella and nasion: (**0.521**, **0.608**), (**0.586**, **0.337**). **</step-1-answer> <step-2-reasoning>** Next, I must identify the relative coordinates of nasion and supramentale that define line 2, in the same format: (x1_line2, y1_line2), (x2_line2, y2_line2). **</step-2-reasoning> <step-2-answer>** The relative coordinates of nasion and supramentale: (**0.586**, **0.337**), (**0.277**, **0.337**). **</step-2-answer> <step-3-reasoning>** I now calculate the angle between the two lines using the pixel dimensions (pixel_width, pixel_height) = (**0.476**, **0.384**), the image size (image_width, image_height) = (**504**, **504**), and the angle formula: angle = arccos(|A · B| / (||A|| ||B||), where A and B are the vectors of the two lines computed from the physical coordinates of their endpoints. A = ((x2_line1 - x1_line1) * image_width * pixel_width, (y2_line1 - y1_line1) * image_height * pixel_height) = ((**0.586** - **0.521**) * **504** * **0.476**, (**0.337** - **0.608**) * **504** * **0.384**) = (15.800, -52.500). B = ((x2_line2 - x1_line2) * image_width * pixel_width, (y2_line2 - y1_line2) * image_height * pixel_height) = ((**0.277** - **0.586**) * **504** * **0.476**, (**0.337** - **0.337**) * **504** * **0.384**) = (-74.000, -0.100). Denote A=(Ax, Ay) and B=(Bx, By). Then, angle = arccos(|Ax*Bx + Ay*By| / (sqrt(Ax^2 + Ay^2) * sqrt(Bx^2 + By^2))) = arccos(|15.800*-74.000 + -52.500*-0.100| / (sqrt(15.800^2 + -52.500^2) * sqrt(-74.000^2 + -0.100^2))) = 1.370 = **78.449** degrees. **</step-3-reasoning> <step-3-answer>** The angle: **78.449**. **</step-3-answer> </think> <answer>** **78.449** **</answer>**



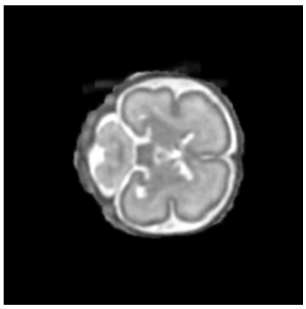
[GT / Prediction / Metrics]

Ground Truth: 70.062 °
Prediction: **78.449** °
Localization Error (line 1 endpoints): normazlied L2 distance = 0.0207
Localization Error (line 2 endpoints): normalized L2 distance = 0.0246
Arithmetic Error (angle): 0.0698 (model: **78.4490** | python evaluator: 73.3281)
Measurement Error (angle): MRE = 0.1197

Figure 9: An example of response from MedVision-V0 for angle measurement.

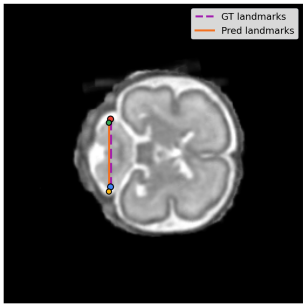
[Prompt]

Task:
Given the input medical image, estimate the distance of transverse cerebellar diameter in millimeters, which is the distance between 2 landmark points: (landmark 1) most right point of cerebellar hemisphere, (landmark 2) most left point of cerebellar hemisphere.
Additional information:
The image size is 504 pixels (width) x 504 pixels (height).
The pixel size for this image is 0.258 mm (width) x 0.258 mm (height).
Format requirement:
The final answer must be enclosed within <answer> </answer> tags. The answer should be a single decimal number without units or extra text.
Reasoning steps:
Step 1: Identify the landmark 1 and record its relative coordinates in the format (x, y) = (relative position in width direction, relative position in height direction). Denote the coordinates as (x1, y1). Step 2: Identify the landmark 2 and record its relative coordinates in the same (x, y) format. Denote the coordinates as (x2, y2). Step 3: Given the pixel dimensions (pixel_width, pixel_height) and image size (image_width, image_height), compute the physical distance between the two landmarks using: distance = sqrt(((x2 - x1) * image_width * pixel_width)^2 + ((y2 - y1) * image_height * pixel_height)^2). Report the reasoning process and final answer within <think> </think> and <answer> </answer> tags, respectively. Inside <think> </think>, include reasoning and step results using <step-k-reasoning> </step-k-reasoning> and <step-k-answer> </step-k-answer> tags.
Follow the reasoning steps to get the final answer in the required format.



[Response]

<think> <step-1-reasoning> I need to identify most right point of cerebellar hemisphere and output its relative coordinates. The relative coordinates must be written as (x1, y1), where x is the relative position in width and y is the relative position in height. **</step-1-reasoning> <step-1-answer>** The relative coordinates of most right point of cerebellar hemisphere: (**0.350**, **0.375**). **</step-1-answer> <step-2-reasoning>** Next, I must identify most left point of cerebellar hemisphere and output its relative coordinates in the same format: (x2, y2). **</step-2-reasoning> <step-2-answer>** The relative coordinates of most left point of cerebellar hemisphere: (**0.350**, **0.605**). **</step-2-answer> <step-3-reasoning>** I now calculate the distance between the two landmarks using the pixel dimensions (pixel_width, pixel_height) = (**0.258**, **0.258**), the image size (image_width, image_height) = (**504**, **504**), and the distance formula: distance = sqrt(((x2 - x1) * image_width * pixel_width)^2 + ((y2 - y1) * image_height * pixel_height)^2) = sqrt(((**0.350** - **0.350**) * **504** * **0.258**)^2 + ((**0.605** - **0.375**) * **504** * **0.258**)^2) = **27.500**. **</step-3-reasoning> <step-3-answer>** The distance: **27.500**. **</step-3-answer> </think> <answer>** **27.500** **</answer>**



[GT / Prediction / Metrics]

Ground Truth: 29.453 mm
Prediction: **27.500** mm
Localization Error (landmark 1): normazlied L2 distance = 0.0117
Localization Error (landmark 2): normalized L2 distance = 0.0094
Arithmetic Error (distance): 0.0805 (model: **27.5000** | python evaluator: 29.9074)
Measurement Error (distance): MRE = 0.0663 nMAE = 0.0106

Figure 10: An example of response from MedVision-V0 for distance measurement.

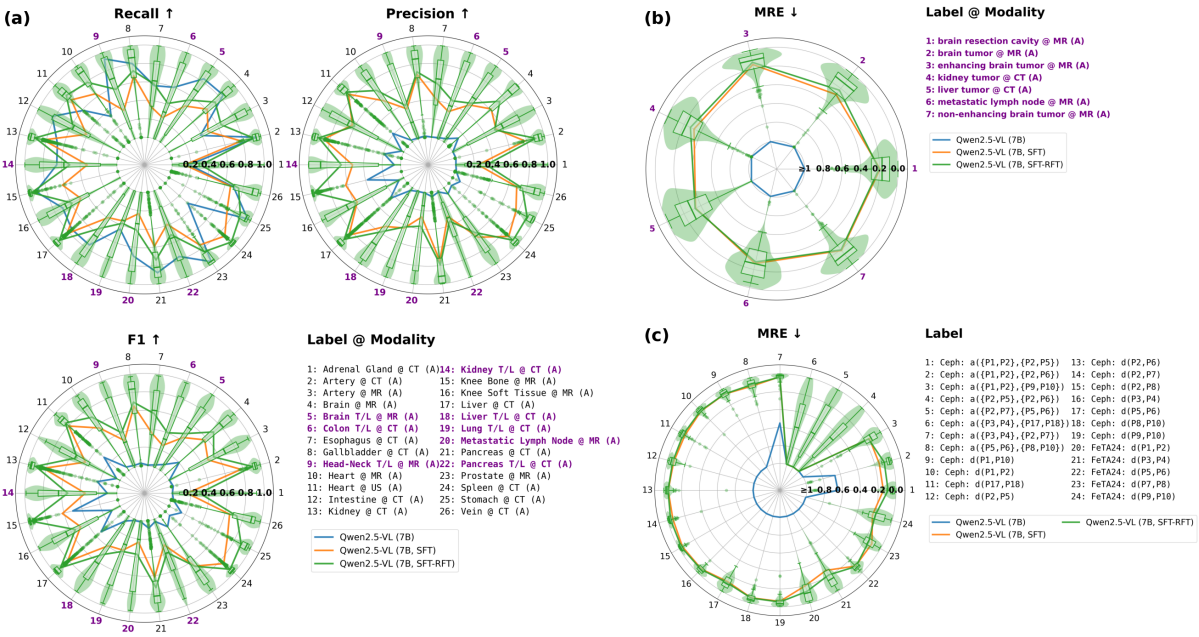


Figure 11: Effectiveness of the SFT-RFT training strategy.



Figure 12: Label level detection performance at each box-image-ratio group.

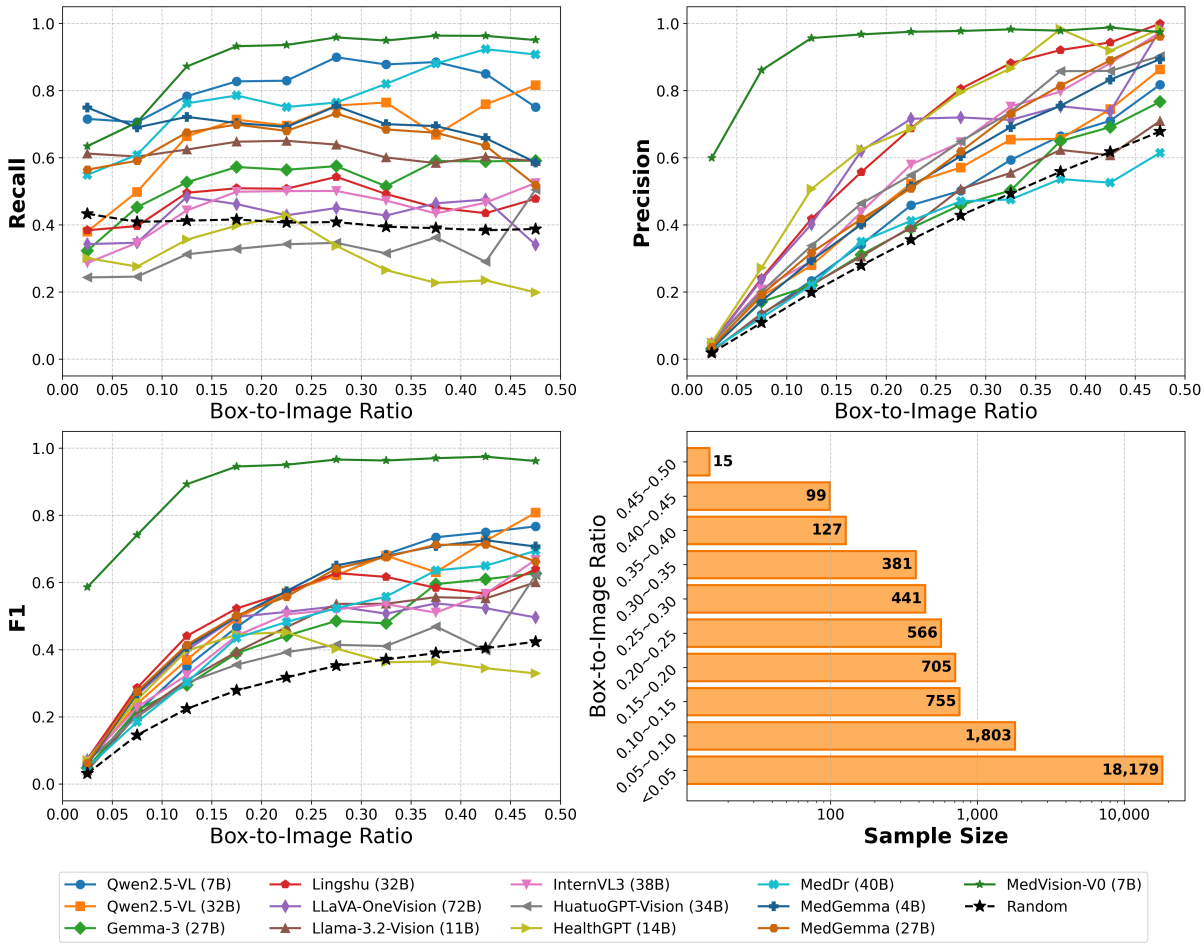


Figure 13: Effect of target size, quantified by box-image-ratio, on detection performance of VLMs.